












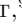






Resolved mass assembly and star formation in Milky Way Progenitors since $z = 5$ from JWST/CANUCS: From clumps and mergers to well-ordered disks

VIVIAN YUN YAN TAN ¹, ADAM MUZZIN ¹, GHASSAN T. E. SARROUH ¹, JACQUELINE ANTWI-DANSO ²,
VISAL SOK ¹, NAADIYAH JAGGA ¹, ROBERTO ABRAHAM ², YOSHIHISA ASADA ^{3,4}, GUILLAUME DESPREZ ⁵,
KARTHEIK IYER ⁶, NICHOLAS S. MARTIS ⁷, ROSA M. MÉRIDA ³, LAMIYA A. MOWLA ⁸, GAËL NOIROT ⁹,
KIYOAKI CHRISTOPHER OMORI ³, MARCIN SAWICKI ³, ROBERTA TRIPODI ⁷ AND CHRIS J. WILLOTT ¹⁰

¹Department of Physics and Astronomy, York University, 4700 Keele Street, Toronto, ON, M3J 1P3, Canada

²David A. Dunlap Department of Astronomy and Astrophysics, University of Toronto, 50 St. George Street, Toronto, Ontario, M5S 3H4, Canada*

³Department of Astronomy and Physics and Institute for Computational Astrophysics, Saint Mary's University, 923 Robie Street, Halifax, Nova Scotia B3H 3C3, Canada

⁴Department of Astronomy, Kyoto University, Sakyo-ku, Kyoto 606-8502, Japan

⁵Kapteyn Astronomical Institute, University of Groningen, P.O. Box 800, 9700AV Groningen, The Netherlands

⁶Columbia Astrophysics Laboratory, Columbia University, 550 West 120th Street, New York, NY 10027, USA

⁷Faculty of Mathematics and Physics, Jadranska ulica 19, SI-1000 Ljubljana, Slovenia

⁸Whitin Observatory, Department of Physics and Astronomy, Wellesley College, 106 Central Street, Wellesley, MA 02481, USA

⁹Space Telescope Science Institute, 3700 San Martin Drive, Baltimore, Maryland 21218, USA

¹⁰National Research Council of Canada, Herzberg Astronomy & Astrophysics Research Centre, 5071 West Saanich Road, Victoria, BC, V9E 2E7, Canada

ABSTRACT

We present a resolved study of > 900 progenitors of Milky Way Analogs (MWAs) at $0.3 < z < 5$ selected with abundance matching in the ten fields of the Canadian NIRISS Unbiased Cluster Survey (CANUCS). Utilizing 18-21 bands of deep NIRCам, NIRISS, and HST photometry, we create resolved stellar mass maps and star formation rate maps via spectral energy distribution fitting with Dense Basis. We examine their resolved stellar mass and specific star formation rate (sSFR) profiles as a function of galactocentric radius, and find clear evidence for inside-out mass assembly. The total M_* of the inner 2 kpc regions of the progenitors remain roughly constant ($10^{9.3-9.4} M_\odot$) at $2 < z < 5$, while the total M_* of the regions beyond 2 kpc increases by 0.8 dex, from $10^{7.5} M_\odot$ to $10^{8.3} M_\odot$. Additionally, the sSFR of the outer regions increase with decreasing redshift, until $z \sim 2$. The median Sérsic index of the MWA progenitors stays nearly constant at $n \sim 1$ at $2 < z < 5$, while the half-mass radii of their stellar mass profiles double. We perform additional morphological measurements on the stellar mass maps via the Gini-M20 plane and asymmetry parameters. They show that the rate of double-peak mergers and disturbances to galaxy structure also increase with redshift, with $\sim 50\%$ of galaxies at $4 < z < 5$ classified as disturbed, and $\sim 20\%$ classified as ongoing mergers. Overall, the early evolution of MWAs is revealed as chaotic, with significant mergers and high SFRs. Mass growth is primarily inside-out and galaxies become more disk-like after $z = 3$.

Keywords: galaxies:evolution, galaxies:high-redshift, galaxies:interactions, milky way

1. INTRODUCTION

The present-day Milky Way is a large spiral galaxy with a total stellar mass of $\sim 5 \times 10^{10} M_\odot$ (see Bland-Hawthorn & Gerhard 2016; Helmi 2020 for reviews). It contains a thin disk with ongoing star formation, a

dynamically hotter thick disk with older stars of lower metallicity (e.g. Bensby et al. 2003; Fuhrmann 2011; Licquia & Newman 2015; Kilic et al. 2017), and a central region with a bar and a pseudobulge (e.g. Shen et al. 2010; Wegg & Gerhard 2013; Wegg et al. 2015; Portail et al. 2017; Barbuy et al. 2018). Stellar streams in the Milky Way's halo reveal remnants of galaxies

* Banting Postdoctoral Fellow

that merged with the Milky Way (Helmi et al. 2018; Belokurov et al. 2018; Horta & Schiavon 2024).

Compared to its peers of similar stellar mass, the Milky Way (MW) can either be typical, or somewhat abnormal. Work from Licquia et al. (2016) shows that the MW lies on the Tully-Fisher relation for galaxies (Tully & Fisher 1977). Fraser-McKelvie et al. (2019) finds the MW lies within two standard deviations of the star-forming main sequence (see Speagle et al. 2014; Schreiber et al. 2015; Santini et al. 2017), however its star formation rate is more consistent with a galaxy transitioning from star-forming to quiescent, green valley galaxy (Mutch et al. 2011). Its disk length scale is also more compact physically compared to other spirals of the same stellar mass (Bovy & Rix 2013; Licquia et al. 2016). Depending on selection criteria, there exists dozens to potentially hundreds of Milky Way Analogs (MWAs) in the local universe, in terms of the galaxies’ mass, morphology, and star formation rate (e.g. Fraser-McKelvie et al. 2019; Kormendy & Bender 2019; Boardman et al. 2020a; Zhou et al. 2023). By comparing the physical characteristics of the MW to its analogs (e.g. Bovy & Rix 2013; Licquia et al. 2016; Boardman et al. 2020b), we gain a better understanding of the MW as it exists in its current state. However, the galaxies of the present-day universe had complex formation histories that we have only begun to glimpse from the current era of high-redshift observations.

Recent studies of gravitationally lensed arcs via multi-band photometry and spectroscopy from JWST reveal very high redshift, reionization era galaxies that are progenitors of many of the galaxies that we find in the local universe. Among these are the Sunrise arc (Vanzella et al. 2023) at $z \sim 5.9$ with a total stellar mass of $10^6 - 10^7 M_\odot$, the Firefly Sparkle (Mowla et al. 2024) at $z \sim 8.3$ with a total stellar mass of $10^{5.3} - 10^{6.3} M_\odot$, and the Cosmic Gems arc (Adamo et al. 2024; Bradley et al. 2024) at $z \sim 10.2$ with a total stellar mass of $10^{7.38} - 10^{7.75} M_\odot$. These correspond to a lookback time of ~ 12.7 Gyr, ~ 13.1 Gyr and ~ 13.3 Gyr respectively. These galaxies are gravitationally bound star clusters with extremely high star formation rates. Although these high- z protogalaxies are a far cry from the “grand-design” spiral disks observed in the local universe, they represent the earliest stages of galaxy formation, and fall within the stellar mass range of possible progenitors of MWAs.

A recent simulation study from Rusta et al. (2024) has shown that the Firefly Sparkle’s stellar mass and star formation history are consistent with that of a MW type galaxy. They provide evidence for the hierarchical assembly model of structure formation in the early uni-

verse (White & Rees 1978), supported by studies of the chemical and kinematic properties of stars in the galactic halo of the MW (e.g. Tumlinson 2010; Salvadori et al. 2010; Belokurov et al. 2018; Belokurov & Kravtsov 2022; Xiang & Rix 2022). Hierarchical assembly also fits with the most widely accepted model of the MW’s formation, the so-called “inside-out” model, which posits the bulge formed first, with the disk and halo coalescing around it (see van den Bosch 1998; Abadi et al. 2003; Muñoz-Mateos et al. 2007; Wang et al. 2011; Licquia et al. 2015; Goddard et al. 2017).

With the advent of next generation high resolution hydrodynamical galaxy simulations such as TNG50 (Pillepich et al. 2019, 2023), FIRE (Hopkins 2015; Oñorbe et al. 2015; Wetzel et al. 2016; Hopkins et al. 2018; Garrison-Kimmel et al. 2018), EAGLE (Schaye et al. 2015; Bignone et al. 2019), and NIHAO-UHD (Buck et al. 2020), we are now able to observe the formation of MW and M31-sized galaxies within these simulations on the sub-kpc scale, along with more complex interactions, such as the survival of the galactic disk after major and minor mergers (Sotillo-Ramos et al. 2022), or satellite galaxies that are gravitationally bound to MW and M31 analogs (Engler et al. 2023). It is now possible to verify the results from these state-of-the-art hydrodynamical simulations by comparison with spatially resolved observations from the high redshift universe (i.e. Giménez-Arteaga et al. 2023; Estrada-Carpenter et al. 2024). As we have an enormous wealth of data from JWST of many epochs from the early universe, we also have a unique opportunity to link the high- z and low- z universe via an *observational* approach. Now in the JWST era, with deep, high-resolution, multiwavelength surveys, one can trace the evolution of disk galaxies further back in time. For example, Le Conte et al. (2024) used the CEERS survey to trace the evolution of resolved galaxy structures such as bars in disks from $1 < z < 3$.

Previous studies which use observations to study MWA progenitors used rest-frame optical and NIR flux from HST as a proxy for stellar mass (van Dokkum et al. 2013; Patel et al. 2013, and Papovich et al. 2015), and the maximum redshift reached was $z \sim 3$. Tan et al. (2024) performed the first resolved mass assembly study but was limited to only $z \sim 2$. In all of these studies, the main disks have already formed by $z \sim 2.5$. A recent study using JWST photometry from Costantin et al. (2023) has also found a MWA at $z \sim 3$ with its disk already formed. Thus, the results from these studies favor neither inside-out nor outside-in models of formation, and the effect of galaxy interactions and mergers on mass assembly was not well explored. Galaxy mergers

are known to play a role in the evolution of the MW (i.e. the last major merger of our galaxy, Gaia-Enceladus, see Belokurov et al. 2018; Helmi et al. 2018), but how common mergers are at different epochs of cosmic time, and how they may drive other processes in addition to mass assembly, such as starbursts or morphological disturbances are less well understood.

In this paper, by utilizing the data from the Canadian NIRISS Unbiased Cluster Survey (CANUCS), we extend the study of spatially resolved galaxy mass assembly to $z \sim 5$. In doing so, we are able to provide a more holistic picture of MWA formation from its earliest steps to the present day. This paper is organized as follows: Section 2 provides a summary of the catalogs used and the selection criteria for MWA progenitors via abundance matching. Section 3.3 describes the process of creating resolved stellar mass and star formation rate maps of our sample of MWA progenitors with SED-fitting using Dense Basis. Section 4 demonstrates the evidence for inside-out growth of MWA progenitors from $2 < z < 5$, and lockstep growth at $0 < z < 2$ from mass density and specific star formation rate densities. Section 5 examines the morphological evolution of MWA progenitors from chaotic, disturbed systems to rotationally supported disks. For this work we assume a Λ CDM cosmology with $\Omega_\Lambda = 0.7$, $\Omega_m = 0.3$, and $H_0 = 70$ km/s/Mpc. We assume a Chabrier (2003) IMF.

2. DATA & SAMPLE SELECTION

2.1. Survey Design

We use the observations from the Canadian NIRISS Unbiased Cluster Survey (CANUCS, see Willott et al. 2022) for its excellent depth at high- z and extensive photometric sampling. There are two fields for each cluster in CANUCS: CLU denotes the cluster field, and NCF denotes the “NIRCam Flanking” field. For the CLU fields, the JWST NIRCam filters used are F090W, F115W, F150W, F200W, F277W, F256W, F410M, and F444W. For the NCF fields, the same wide band filters are also used, *except for* F200W. Additionally, NCF fields are imaged by the medium band NIRCam filters F140M, F162M, F182M, F210M, F250M, F300M, F335M, F360M, and F410M. All imaging information for each field is described in Table 1. Details of PSF-matching and catalog creation for CANUCS are described in Willott et al. (2024) and Sarrouh et al. (2024). Source detection and aperture photometry was done using the Photutils package from astropy (Bradley et al. 2016, 2023) as described in Asada et al. (2024a). See §3.1 for typical aperture size used for each object in this work, and additional details on resolved photometry.

For this work, we only make use of the photometric data. Additional imaging from HST/ACS and HST/WFC3 are provided in the filters F435W, F606W, F814W, F105W, F110W, F125W, and F160W for fields that overlap with the Hubble Frontier Fields survey (Lotz et al. 2017), i.e. both CLU and NCF for Abell 370, MACS 0416, MACS 1149, as well as MACS0417CLU and MACS1423CLU. However, for MACS0417NCF and MACS1423NCF, there is no ACS imaging, so imaging in the bluest bands is provided by WFC3/UVIS in the bands F438WU and F606WU. For exact usage of bands, and catalog version, see Table 1.

2.2. Data Reduction

Image processing and catalog construction will be discussed in detail in Sarrouh and Asada et al. (in prep.), which we briefly describe here. For more information on the data reduction process for CANUCS, we refer the reader to Noirot et al. (2023). The full CANUCS dataset includes NIRCam photometry, with spectroscopy from NIRISS and NIRSpec of five strong lensing clusters Abell 370, MACS J0416.1-2403 (hereafter MACS 0416), MACS J0417.5-1154 (hereafter MACS 0417), MACS J1149.5+2223 (hereafter MACS 1149), and MACS J1423.8+2404 (hereafter MACS 1423).

In general, the NCF fields are deeper than the cluster fields by 0.3 to 0.6 magnitudes for the same band. The shallowest median depth (3σ in 0.3” apertures) is 27.2 mag in the HST bands of F125W and F140W for MACS 0417 CLU, and the deepest median depth is the JWST NIRCam band of F277W in MACS 1149 NCF, at 30.8 mag (3σ in 0.3”, see Desprez et al. 2024; Asada et al. 2024a, and Willott et al. 2024 for more information). The cluster fields are affected by gravitational lensing, albeit at different strengths for different clusters. Any object in the catalogs with a best-fit model lensing magnification of $\mu > 2.5$ are excluded from the selection. The Abell 370 cluster field is the field impacted the most by lensing overall, and thus our sample is the smallest in that field. The lensing models for Abell 370 are provided in Gledhill et al. (2024), for MACS0416 in Rihtaršič et al. (2024), MACS1149 in Rhitaršic et al. (in prep), and MACS 0417 and MACS 1423 in Desprez et al. (in prep).

The full CANUCS catalog is complete to AB magnitude 27 in the reddest filter F444W at all redshifts (including this work’s redshift limit of $z \sim 5$). However, the signal-to-noise cutoff necessary for successful Voronoi binning is $S/N > 30$ in F444W. This signal-to-noise threshold is set to ensure that the individual spatial bins have $S/N > 5$. This means that out of all possible MWAs in the CANUCS fields, only the bright-

Table 1. The catalog version and list of all NIRCcam and HST filters used for each respective CANUCS field in this work. Note that the cluster fields (CLU) also contain additional NIRISS photometry in the bands *F115WN*, *F150WN*, and *F200WN*, which is included in the count of total number of filters.

Field	Catalog version	NIRCcam	HST	Total number of filters
MACS0417CLU	v1p0.3	F090W, F115W, F150W, F200W, F277W, F356W, F410M, F444W	F435W, F606W, F814W, F105W, F125W, F140W, F160W	18
Abell370CLU	v1p1.1	F090W, F115W, F150W, F200W, F277W, F356W, F410M, F444W	F435W, F606W, F814W, F105W, F110W, F125W, F140W, F160W	19
MACS0416CLU	v1p1.1	F090W, F115W, F150W, F200W, F277W, F356W, F410M, F444W	F435W, F606W, F814W, F105W, F110W, F125W, F140W, F160W	19
MACS1423CLU	v1p0.1	F090W, F115W, F150W, F200W, F277W, F356W, F410M, F444W	F435W, F606W, F814W, F105W, F110W, F125W, F140W, F160W	19
MACS1149CLU	v1p2.1	F090W, F115W, F150W, F200W, F277W, F356W, F410M, F444W	F435W, F606W, F814W, F105W, F110W, F125W, F140W, F160W	19
MACS0417NCF	v1p0.2	F090W, F115W, F140M, F150W, F160M, F182M, F210M, F250M, F277W, F300M, F335M, F360M, F410M, F444W	F438WU, F606WU	16
Abell370NCF	v2p0.1	F090W, F115W, F140M, F150W, F160M, F182M, F210M, F250M, F277W, F300M, F335M, F360M, F410M, F444W	F435W, F606W, F814W, F105W, F125W, F140W, F160W	21
MACS0416NCF	v1p1.1	F090W, F115W, F140M, F150W, F160M, F182M, F210M, F250M, F277W, F300M, F335M, F360M, F410M, F444W	F435W, F606W, F814W, F105W, F125W, F140W, F160W	21
MACS1423NCF	v1p0.1	F090W, F115W, F140M, F150W, F160M, F182M, F210M, F250M, F277W, F300M, F335M, F360M, F410M, F444W	F438WU, F606WU, F125W, F160W	18
MACS1149NCF	v1p2.1	F090W, F115W, F140M, F150W, F160M, F182M, F210M, F250M, F277W, F300M, F335M, F360M, F410M, F444W	F435W, F606W, F814W, F105W, F125W, F140W, F160W	19

est at high- z can be retained in our sample. More information on Voronoi binning is provided in §3.1. Photometric redshifts in the CANUCS catalog (Asada et al. 2024a,b) were obtained with an implementation of EAZY in Python known as *eazy-py* (Brammer et al. 2008). During fitting, a systematic flux error of 5% was added in quadrature to the nominal photometric uncertainty.

2.3. Sample Selection via Abundance Matching

Selecting MWA progenitors may be done via abundance matching, or using properties from simulations (such as stellar masses, halo masses, star-formation history, etc.) as a standard. We choose to use abundance matching, but we demonstrate that both methods are consistent in Figure 1. To estimate the range of stellar masses of progenitors of MW-mass galaxies at higher redshift, we assume an evolving co-moving number density with redshift, as determined in Behroozi et al. (2013), with a present day number density of $\log(n/\text{Mpc}^3) = -2.95$ for MWs. This number density corresponds to a MW stellar mass of $10^{10.7} M_\odot$ at $z = 0$. The code calculates a past median galaxy number density at z_2 , given an initial number density at z_1 , via peak halo mass functions. Since the merger rate per unit halo per unit Δz is roughly constant, the evolution of cumulative number density of progenitors of any given galaxy is a power law, with the change described by $0.16 \times \Delta z$ dex. Behroozi et al. (2013) uses peak halo mass functions for which the resultant median number densities are less affected by the scatter in stellar mass and luminosity. However, this scatter does affect the 1σ errors in cumulative number density. The 1σ or 68 percentile range grows with increasing redshift. The 1σ values grow by ~ 0.16 dex per 0.5 change in redshift.

Behroozi et al. (2013) does not assign stellar masses to the number densities, but rather determines the number density of the median *halo* mass. Thus, we obtain the stellar mass ranges of the MWA progenitors using the same number densities from the stellar mass functions (SMFs) from two studies, Grazian et al. (2015) and McLeod et al. (2021). Both studies used a combination of ground-based and HST data: Grazian et al. (2015) CANDELS-UDS, GOODS-South, and HUDF09 and HUDF12. The surveys used by McLeod et al. (2021) are a combination of UKIDSS Ultra Deep Survey, UltraVISTA, CFHTLS-D1, and all five CANDELS fields. The result of this matching of cumulative number densities for MWs to median stellar masses is shown in the top panel of Figure 1. A similar analysis is done in Tan et al. (2024) for the Hubble Frontier Fields but with SMFs from Muzzin et al. (2013). See Mowla et al.

(2024) for the extension of this abundance matching in CANUCS to $5 < z < 9$.

We take the median cumulative number densities at each Δz , to find the stellar mass associated with that number density from the corresponding SMF. In addition, the 1σ errors on the given number density for each redshift are used to determine the maximum and minimum boundaries on the stellar mass of the progenitors at each epoch. Galaxies with redshifts within ± 0.05 of the cluster’s redshift are removed from our sample to prevent contamination from cluster galaxies. The full sample is plotted in the bottom panels of Figure 1. Also shown in Figure 1 are comparisons of this sample’s median stellar mass and 1σ stellar mass range to past works that have studied progenitors of MWs. The left panel focuses primarily on studies that used observational data (van Dokkum et al. 2013; Patel et al. 2013; Papovich et al. 2015; Tan et al. 2024), while the right panel primarily focuses on studies with simulations (Guedes et al. 2011; Grand et al. 2017; Moster et al. 2018; Garrison-Kimmel et al. 2018; Buck et al. 2020; Pillepich et al. 2023). The TNG50 results from Pillepich et al. (2023) are plotted in both panels for comparison. Our stellar mass range for each redshift bin for MWA progenitors agree with the literature, for both observations and simulations.

In Figure 2, we apply the selection criteria as described above to the CANUCS catalogs, and plot the catalog stellar mass versus redshift in the top panel, and the catalog instantaneous SFR versus redshift in the bottom panel (unlike the photometric catalogs, the mass catalogs are obtained with Dense Basis, see §3.3 for more details). Note the CANUCS catalog stellar mass and instantaneous SFR (henceforth simply called ‘SFR’) are integrated over the whole galaxy. The color of the points show their integrated sSFR (SFR/stellar mass). The vast majority of galaxies have $\log(\text{sSFR}) > -11$. Due to the relationship between stellar mass and redshift, lower- z galaxies tend to be more massive but have lower sSFR than higher- z galaxies with the same total SFR.

There are 5307 potential MWA progenitor galaxies at $0 < z < 5$ that fall within the 1σ boundaries as defined by applying the abundance matching code to the given SMFs. In this paper, we SED-fit galaxies in 2D, and an integrated $S/N > 30$ is required to get meaningful, spatially-resolved SED fits. Therefore, the colored dots represent the subsample of these potential MWA progenitors that have a $S/N > 30$ in their integrated F444W flux. This ensures that each spatial bin will have at least $S/N = 5$ at higher redshifts, and ensures there are at least 50 spatial bins per galaxy. We remove the small grey points from our sample, which have inte-

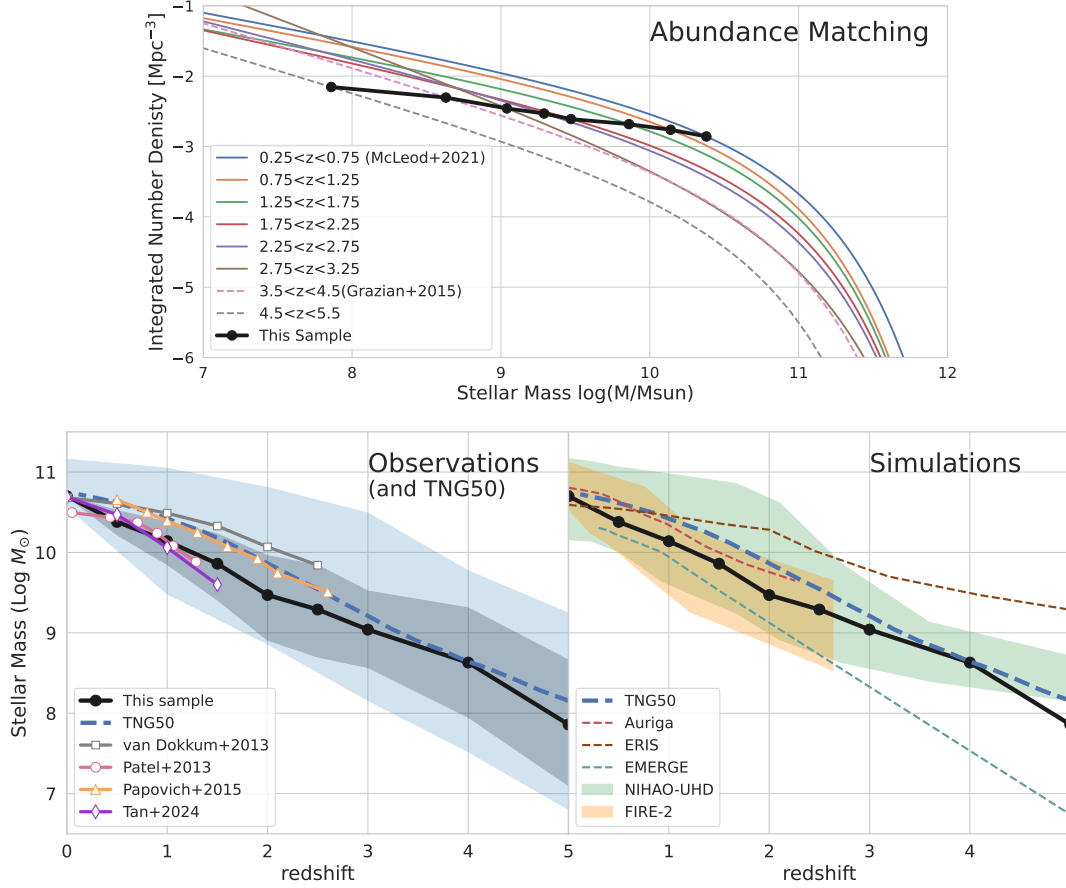


Figure 1. *Top Panel:* Each black point represents the intersection between the cumulative number density predicted by abundance matching (Behroozi et al. 2013) for MWA progenitors, and the stellar mass corresponding to that number density given by the stellar mass function (SMF) at that redshift interval. The starting point is a number density of 0.0011 Mpc^{-3} at $z = 0$, corresponding to $M_{\star} = 10^{10.7} M_{\odot}$. Solid SMFs are from McLeod et al. (2021), dashed SMFs are from Grazian et al. (2015). *Bottom left:* Median stellar mass versus redshift for MWA progenitors plotted in black points. The shaded grey region is the 1σ deviation (16th to 84th percentile) of our sample, which comes from the 1σ range in number density from the abundance matching code. We compare our median stellar mass to the median stellar mass from TNG50 (Sotillo-Ramos et al. 2022; Pillepich et al. 2023) represented with the blue dashed line. The blue shaded region is the TNG50 sample’s 10th to 90th percentile. Previous *observation-based* studies (van Dokkum et al. 2013; Patel et al. 2013; Papovich et al. 2015; Tan et al. 2024) are also plotted in grey with white points. *Right panel:* Comparison of this sample’s stellar mass evolution for MW progenitors versus predictions from various simulations, such as TNG50, again in blue, Auriga (Grand et al. 2017), ERIS (Guedes et al. 2011), EMERGE (Moster et al. 2018), FIRE-2 (Garrison-Kimmel et al. 2018), and NIHAO-UHD (Buck et al. 2020).

grated $S/N < 30$. After additionally removing 23 more galaxies on the basis of missing photometry in all JWST bands bluer than F250M (which would make the SED fit untrustworthy for resolved modeling), our full sample of MWA progenitors for 2D SED modeling is a total of 909 galaxies.

A result of this signal-to-noise cutoff is that the higher mass galaxies at higher- z are selected over lower mass galaxies. As shown in Figure 2, our sample is complete to $z = 3$. Above $z = 3$, we become increasingly biased towards more massive progenitors. In addition, the median SFR, as plotted in the bottom panel of Figure 2, no longer peaks at $z \sim 1.5$, but continues to rise to $z \sim 5$. Ultimately, the CANUCS dataset is among the deep-

est JWST surveys to date, and we continue the analysis to $z = 5$. Note that at $z > 3$, there is an increasing degree of progenitor bias in the results. In order to be complete at $z = 5$ would require an order of magnitude more depth, which can only be obtained with two orders of magnitude greater exposure time. Given that the CANUCS integration times are $\sim 1 - 3$ hours, this is unlikely to be obtained within the mission (see Willott et al. 2022). Strong lensing samples, such as the Firefly and Cosmic Gems, are necessary for even higher redshifts, though they are limited in number for each lensing cluster. Thus, our sample shows a “first look” at evolution of progenitors up to $z = 5$.

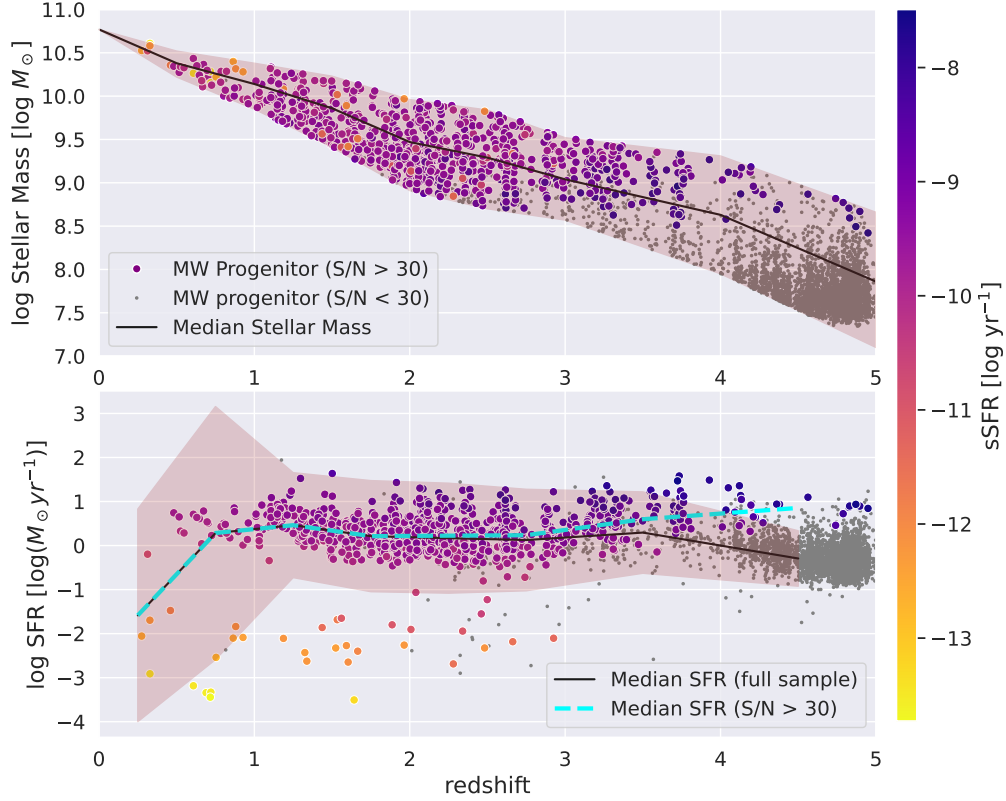


Figure 2. *Top panel:* Integrated stellar masses (obtained with Dense Basis) versus photometric redshift of MWA progenitors in the CANUCS fields selected by abundance matching and SMFs. The solid black line is the rolling median of the stellar mass for each redshift range, and corresponds to the solid black line in Figure 1, while the shaded red region represents the 1σ scatter, same as the shaded grey region in Figure 1. Large colored points are galaxies that have $S/N > 30$, and their color represents the specific SFR. The small grey points have too little signal-to-noise for resolved photometry, and are excluded from our final sample. *Bottom panel:* Catalog log SFR vs Redshift, same selection criteria as above. The shaded red region represents the 1σ scatter of SFR. The color of each point indicates specific SFR. Note that at higher redshifts, galaxies with $S/N > 30$ skew towards the higher mass and higher SFR end of the full distribution of possible MWAs in that redshift range. Note that quiescent galaxies are not used for the main analysis.

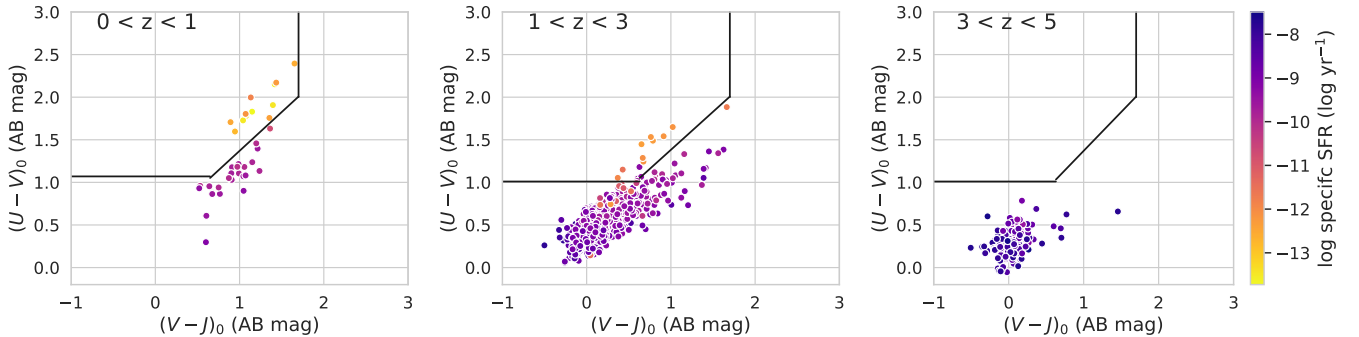


Figure 3. The distribution of UVJ colors for the MWA progenitors. Since the quiescent fraction of MWAs is small ($\sim 0.03\%$), The UVJ boundaries are defined with a bimodal distribution of 9615 galaxies in CANUCS at $0 < z < 5$, with a 25% quiescent fraction (See Appendix A). The color calibration is adapted from Antwi-Danso et al. (2023). The color of the points represent the sSFR of the MWA progenitor sample.

2.4. Quiescent fraction in the MWA sample

A limitation of abundance matching is that not all selected progenitors will evolve into an MWA at $z = 0$. Since the MW is still star-forming (albeit with a much lower star formation rate that places it within the Green Valley, see [Mutch et al. 2011](#)), we only select actively star-forming galaxies within our MWA progenitor sample for an accurate picture of the mass assembly relevant to the MW itself. Even though any actively star-forming higher- z may become quiescent before reaching $z = 0$, quiescent galaxies can certainly be discounted as MWAs. Therefore, we use rest-frame UVJ colors in combination with the sSFR of this sample to find and remove quiescent galaxies.

In Figure 3, we plot the rest-frame colors of our progenitor sample. In order to determine the proper color-magnitude cuts, we utilize the code presented in [Antwi-Danso et al. \(2023\)](#). The code searches for a bimodality in color space by calculating the distance of each galaxy from the UVJ diagonal line. We refit the UVJ slope for the color calibration with the redshift range changed to $0 < z < 5$. For more information on UVJ color calibration, see Appendix A.

The UVJ boundaries for each given redshift epoch are:

$$\begin{aligned} 0 < z < 1 : \quad & (V - J) < 1.7; (U - V) > 1.07; \\ & (U - V) > (V - J) \times 0.91 + 0.67. \quad (1) \\ 1 < z < 5 : \quad & (V - J) < 1.7; (U - V) > 1.01; \end{aligned} \quad (2)$$

We lowered the $(U - V)$ boundary by 0.23 to accommodate a simple stellar population at $z \sim 6$ with an age of ~ 800 Myr. This corresponds to the age of a typical post-starburst galaxy at $0.5 < z < 2.5$ ([Belli et al. 2019; Wild et al. 2020](#)). At $z > 1$, the horizontal line was further lowered by 0.06 magnitudes to better match the sSFR distribution of the MWA progenitors. The divisions presented above are also shown in Figure 3, in each panel, as solid black lines. The color of the points represent the galaxy's sSFR.

After the signal-to-noise cut, and separating the sample into star-forming and quiescent, there are 885 star-forming galaxies, and 24 quiescent galaxies. 12 out of the 24 quiescent galaxies are at $z < 1$. Additionally, there are only star-forming galaxies at $3 < z < 5$.

3. SPATIALLY RESOLVED SED-FITTING ON JWST PHOTOMETRY

In this section, we explain the methods of creating spatially resolved maps of stellar mass and instantaneous SFR distributions for our sample of MWA progenitor galaxies. All resolved photometry is applied to

the science images PSF-matched to F444W provided by CANUCS. The size of the PSF FWHM for the F444W filter is $0.15''$ or 2.3 pixels.

3.1. Voronoi binning of galaxy images

In preparation for resolved SED-fitting, we use Voronoi binning ([Cappellari & Copin 2003](#)) on cutouts of each galaxy. The overall process is similar to the process outlined in previous works [Tan et al. \(2022\)](#) and [Tan et al. \(2024\)](#) using Hubble photometry, however, instead of Voronoi tessellating across the whole of the cutout, the cutouts were separated into two areas: the galaxy, and the background.

The area of the image defined to be the galaxy are the pixels of the cutout contained in an elliptical aperture scaled to the Kron radius of each object via their major and minor axes a and b :

$$R_{model,a} = 2.5R_{kron}a \quad , \quad R_{model,b} = 2.5R_{kron}b \quad . \quad (3)$$

Note that this is the *modified* definition of Kron radius, as defined in Source Extractor and Photutils (see [Bertin & Arnouts 1996](#) and [Bradley et al. 2016](#) for details). As mentioned in §2, the CANUCS photometric catalogs were created with the Photutils package, so a and b multiplied by Kron radius R_{kron} would define an elliptical aperture that contains roughly 68% of the galaxy's light. Therefore, at 2.5 times the Kron radii, the aperture would capture roughly 97% of the galaxy's light within it.

For each field, from the preliminary sample chosen via stellar mass limits from abundance matching, we only select objects to perform pixel-binning if the total integrated flux in the F444W band as defined by the Kron radius of the object has $S/N = 30$ or higher.

In preparation for Voronoi binning, we set the minimum signal-to-noise threshold for the binning within the aperture to be $S/N = 10$ for galaxies at $z < 1.8$, and $S/N = 5$ for galaxies at $z \geq 1.8$. This is to ensure that higher- z galaxies have smaller spatial bins for better resolution. For the pixels outside the aperture in the cutout, the minimum signal-to-noise threshold is set at a value of $S/N = 3$. If binning fails for the background (the pixels outside the aperture), the signal-to-noise is lowered by 1 until a minimum of $S/N = 1$.

3.2. Accurate flux errors for photometric catalogs of Voronoi bins

In order to have resolved stellar mass maps, we must first create a new photometric catalog for the total flux and flux errors in each spatial bin of each cutout of a MWA progenitor in our sample. This ensures that resolved SED-fitting is performed in the same manner for

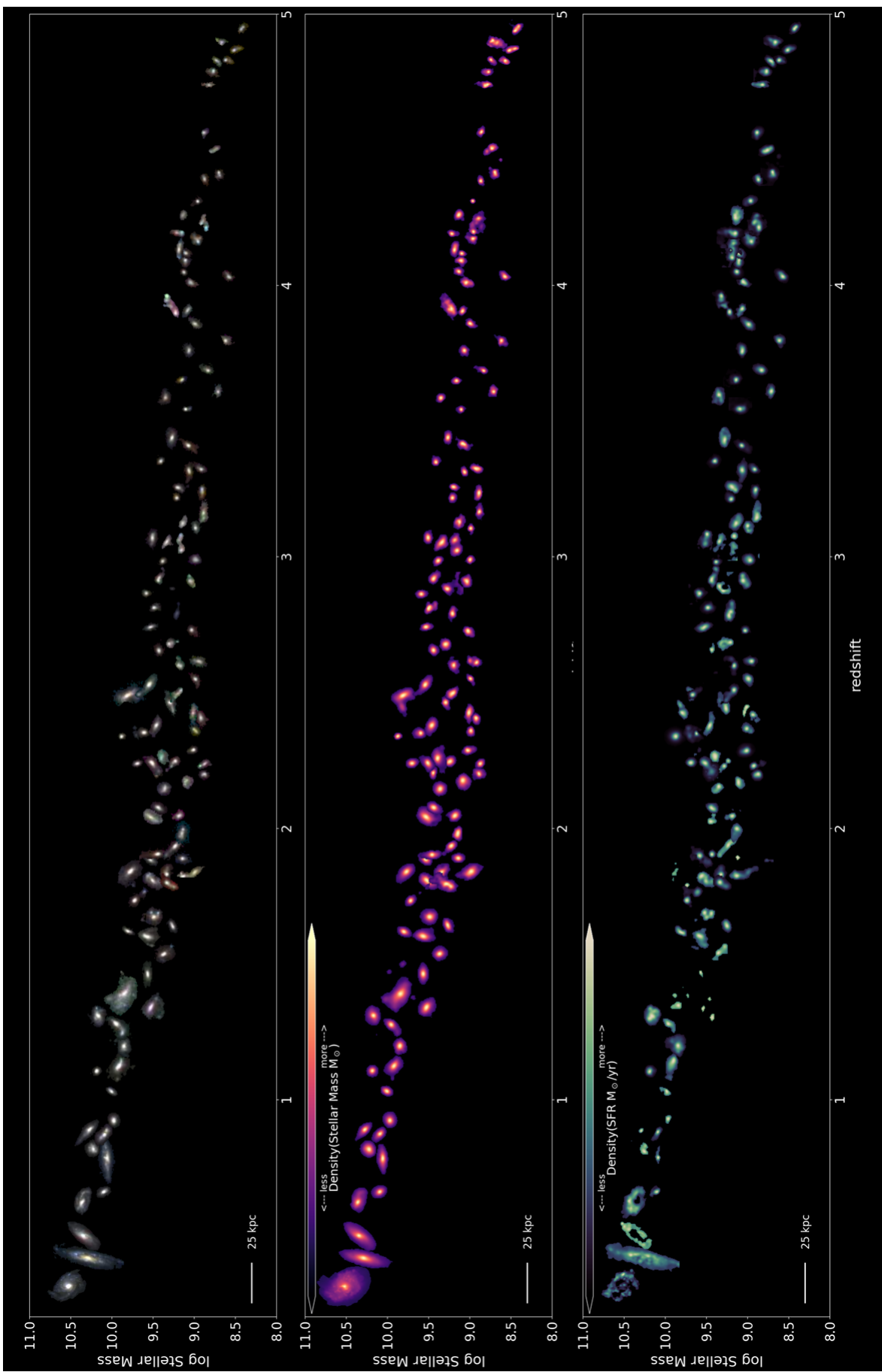


Figure 4. Color images (top panel), resolved stellar mass maps (middle panel), and resolved SFR maps (bottom panel) of a randomly selected subsample of 120 MWA progenitors. The plots are inset into a total stellar mass versus redshift plot to demonstrate the evolutionary trend of the progenitors. Each image has the same physical scale in kpc, displayed in the bottom-left corner. Certain galaxy images are offset by no more than $\pm 0.25z$ or $\pm 0.25 \log M_{\odot}$ to lessen overlap. Note that at higher redshifts, the morphologies shown are not fully representative of the progenitor population.

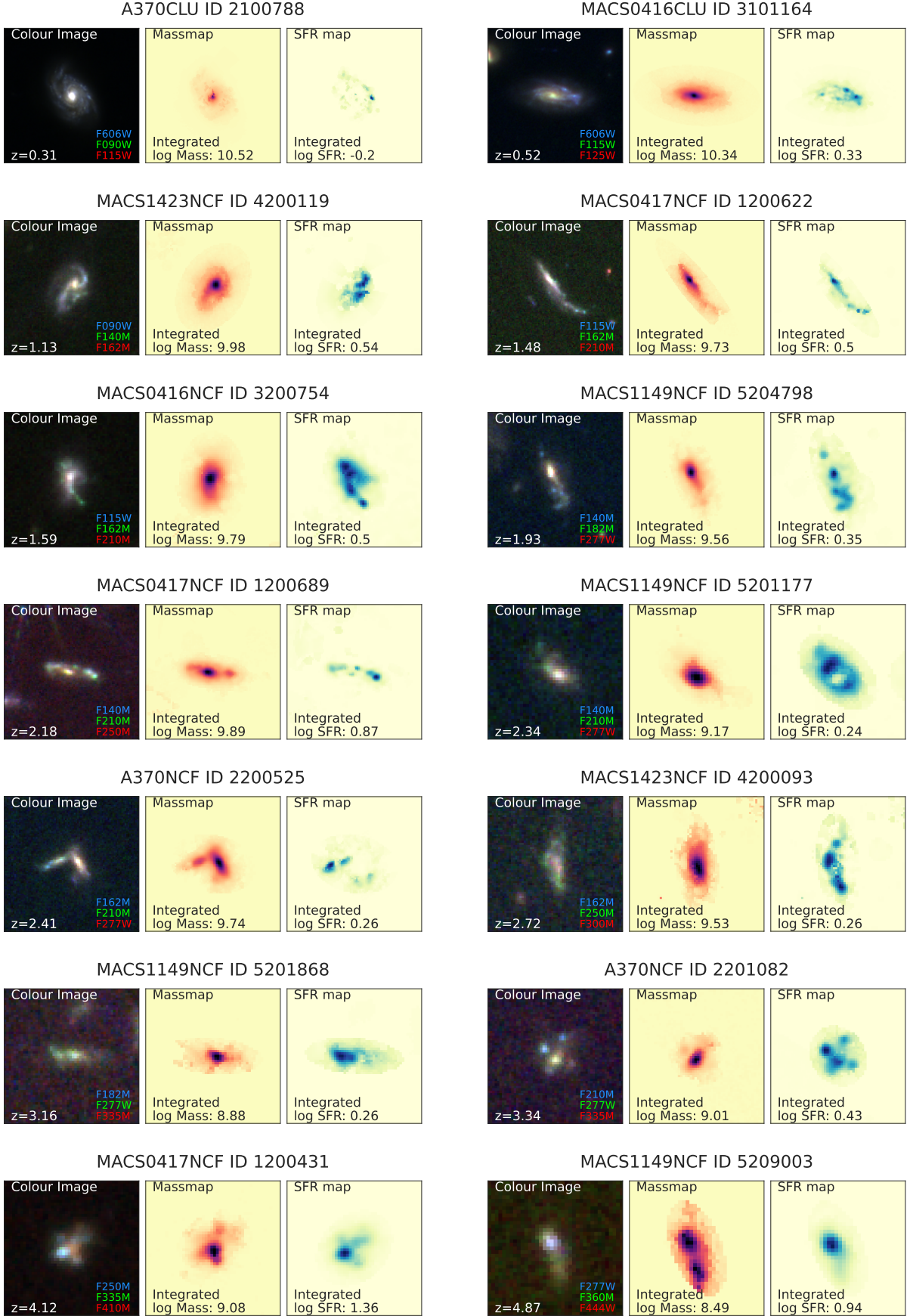


Figure 5. Rest frame *gri* color image, stellar mass map, and SFR map of select MWA progenitors from CANUCS. Units for integrated stellar mass are in $\log(M_{\odot})$ and for integrated SFR are in $\log(M_{\odot}/\text{yr})$. Progenitors are more actively star-forming at higher redshift, and star formation occurs further from the central regions at lower redshift.

this study as it was done on the integrated photometry of the entire CANUCS catalog.

The flux errors for each spatial bin of each galaxy were derived by approximating the size of the bin to a circularized aperture of a specific radius. The longest distance between two pixels in a single bin is taken to be the “diameter” of the aperture. This is because the Voronoi binning algorithm was set to run with both “weighted Voronoi tessellation” (WVT) and “centroidal Voronoi tessellation” (CVT) modes, and thus binned regions are close enough to circular for this distance to be a good approximation. Afterwards, the flux error of the circularized aperture is set as the background flux error for the specified bin. The flux error for the circularized apertures are calculated by taking the FWHM of the number of counts from ~ 2000 empty apertures of the same size placed on empty regions across each respective CANUCS field. This means that every photometric band of every field has its own specific set of background flux errors. Similar to the photometric catalogs and mass catalogs, a systematic error of 3% was added in quadrature to each spatial bin. We chose 3% to be consistent with the mass catalogs of CANUCS, which are also fit with Dense Basis. (See Sarrouh et al. 2024 for more details related to this flux error in application to CANUCS catalog construction. See Sok et al. 2024 and Jagga et al., in prep. for a similar treatment of flux errors in Voronoi binning.)

In addition, the extinction correction factors for each galaxy from the catalog was also applied to the total flux of the pixel bins for each respective galaxy, to ensure that the SED fit is as accurate as possible.

3.3. Creating stellar mass and SFR maps

Similar to the construction of the full CANUCS mass catalogs, we use Dense Basis (Iyer & Gawiser 2017; Iyer et al. 2019) with the FSPS libraries (Conroy & Gunn 2010) to perform SED-fitting to the resolved photometric catalogs created for each individual galaxy in our MWA progenitor sample. Dense Basis is a non-parametric SED-fitting code that uses Gaussian process kernels to fit star formation histories (SFHs). This flexibility makes Dense Basis an ideal SED-fitting code for both obtaining the stellar mass density maps, and creating resolved SFR maps for specific sub-regions of a galaxy. Since higher- z galaxies contain more star-forming clumps, SFR maps can reveal a wealth of information about the mass assembly history of MWA progenitors.

The relevant information for both SED-fitting and SFH reconstruction is saved into an atlas of template SEDs, also called a pregrid, and was done for each cata-

log for the CANUCS fields. By default, Dense Basis uses a Chabrier IMF (Chabrier 2003), and the Calzetti dust law (Calzetti et al. 2000). We choose a flat sSFR prior for the star-formation rate. We use an exponential dust attenuation prior with values of A_V allowed to vary between 0 and 4. We also use a flat metallicity prior with a range of $-1.5 < Z < 0.25$. For SFH reconstruction, the pregrid is given a set of timescales $\{t_x\}$ on which different SFRs are computed (i.e. $\{t_x\} = t_{10}, t_{100}, t_{300}, t_{1000}$ for the CANUCS catalogs). For consistency, we use the instantaneous SFR, which is the average SFR over the time scale at which the galaxy formed the last 1% of its mass.

In order to be consistent with the integrated stellar mass and SFR of the CANUCS catalogs, we use the same pregrid atlases for each respective CANUCS field. When Dense Basis is run on each galaxy, it is run on each spatial bin of the galaxy cutout, treating the bin as an “aperture” itself, with flux and errors distributed accordingly. We fix the redshift for each pixel bin to the photometric redshift of the galaxy. We take the best-fit median stellar mass and median SFR as the resultant stellar mass and SFR for each respective pixel bin. For better resolution in larger bins, we distribute the total stellar mass or SFR of that bin among the pixels depending on how much flux that individual pixel contributed to the total flux of the bin in the relevant band. For stellar mass maps, the filter used to determine distribution of the stellar mass within a single bin is the reddest filter, F444W, whereas for the SFR, the filter used is the closest broadband or medium band filter to rest-frame u -band (365 nm).

In Figure 4, we display 119 randomly chosen examples of the original 909 MWAs and plot their color images, stellar mass maps, and SFR maps inset into a plot of the total stellar mass versus redshift to demonstrate the evolution of the mass density and SFR density over our entire redshift range. The images are scaled to the same angular resolution to demonstrate how much progenitors have grown since $z = 5$. MWA progenitors grow significantly in total mass and size, since $z = 5$, with disk structures emerging around $z \sim 2.5$. In Figure 5, we present more detailed color images, stellar mass maps, and SFR maps of 16 select galaxies from this sample across a variety of redshifts. What is notable about the resolved SFR maps in Figure 5 is that regions of high star formation are closer to and even overlap with regions of high stellar mass density at earlier times, but the star-forming regions migrate further out at later times, decoupled from regions where stellar mass is concentrated. We further investigate these evolution-

ary changes in stellar mass and SFR quantitatively in §4 and §5.

4. RESOLVED MASS ASSEMBLY AND STAR FORMATION OF MWA PROGENITORS

In this section, we show measurements of the growth of MWA progenitors to better understand the mass growth history of the MW. We utilize both mass and sSFR density profiles to track the overall mass assembly since $z = 5$, which spans a time period of 12.5 Gyr. Thus, we group the MWA progenitors into redshift bins according to the redshift ranges represented by the SMFs of McLeod et al. (2021) and Grazian et al. (2015) in §2.3. The stellar mass boundaries of each redshift bin are represented by the grey shaded region in the bottom left panel of Figure 1, as well as the brown shaded region in the top panel of Figure 2. For each redshift bin, a stacked and normalized mass and sSFR radial density profile is created from the individual radial profile (both Σ_{star} and Σ_{sSFR}) of each galaxy. We also further separate the profiles into inner and outer regions, as defined by the positional relation to a galactocentric radius of $R = 2$ kpc. We track the inner, outer, and overall mass growth, sSFR, as well as their respective density over time to quantify the difference in mass growth over cosmic time.

4.1. Density profiles as a function of galactocentric radius

The 1-D mass and SFR density profiles as a function of distance from galactic center R are obtained by placing elliptical annuli centered on the galaxy cutout with a width of 0.1 kpc on the stellar mass and SFR maps. The total stellar mass or SFR within each annulus is then divided by the total area of the annulus. The shape of the annuli are defined by the galaxy's b/a ratio as found in the CANUCS catalogs. Each individual galaxy's mass density or SFR density profile is then sorted according to their redshift bin, then stacked and normalized to obtain the density profile of that redshift. These normalized density profiles are shown in Figure 6, with distances from the center measured along the semi-major axis. See Appendix B for the individual mass and SFR density profiles for each galaxy, divided into redshift bins.

The solid lines of the mass density profiles in the top panel of Figure 6 reveal that at higher redshifts ($2 < z < 5$), mass density increases between different redshift steps more at greater distance from the galactic centre. At $R < 1$ kpc, the increase in mass density from is roughly $\sim 0.1 - 0.2$ dex, from $4 < z < 5$ to $2 < z < 2.5$. At a further distance of $R \sim 2.5$ kpc, the increase in mass density from one redshift epoch to the next is

~ 1 dex, an entire order of magnitude greater. This trend is reflected in the sSFR density profiles as well, as the sSFR starts off relatively flat across the entire normalized profile at $4 < z < 5$, but the highest sSFR consistently occurs at the furthest point from the centre of the galaxy, until $z \sim 0.5$ when it flattens out once more.

If we compare the solid lines (star-forming only profiles) to the dashed lines (star-forming and quiescents) in Figure 6, the main effect of removing quiescents is that the mass density towards the middle 2 kpc of the galaxy is much flatter, and the sSFR density increases by an order of magnitude, and becomes roughly constant with respect to distance from the center R , as opposed to rising with increasing R . This demonstrates that quiescent MWAs at lower redshifts are more bulge-dominated than star-forming galaxies. Note that in §2.4, we discussed the effects of including versus excluding quiescents from the MWA progenitor sample. From the comparison of the profiles, the inclusion of quiescents affects the density profiles primarily at $z < 1$.

At higher redshifts, the mass density profiles retain a similar shape in the center, but their outskirts increase in mass. This might best be shown by the comparison of the growth in the centre ($R < 2$ kpc), to the growth at 4.5 kpc, which is approximately the effective radius of MWA at $z \sim 0$ (see §5.2). Over the redshift range covered by our data the central part of the MWA grows by about an order of magnitude in mass, however, the growth at $R \sim 4.5$ kpc is two orders of magnitude, implying ten times more growth at the effective radius. Likewise, in the sSFR density, while the sSFR is continuously decreasing at later times, the highest sSFR density is usually near the limits of the density profile's boundary, implying that the outskirts of the galaxies are where most of the sSFR is concentrated. This shows that towards lower redshift, galaxies are increasingly growing their disks, which is evidence for inside-out growth.

We note that this trend may be affected by PSF smearing, because the physical kpc scale of the PSF increases up to $z \sim 1.5$ (the affected regions of the density profile have greater transparency in Figure 6). However, since the size of the PSF is never greater than 1 kpc even at the redshift bin with the worst physical resolution, PSF smearing cannot account for all of the density profile changes within $R = 2$ kpc, which is defined as the inner regions of the profiles. Additionally, the total stellar mass and total sSFR in the inner regions should be less affected by the PSF, and how those quantities change with redshift is discussed in the next section.

4.2. Inner regions versus outskirts

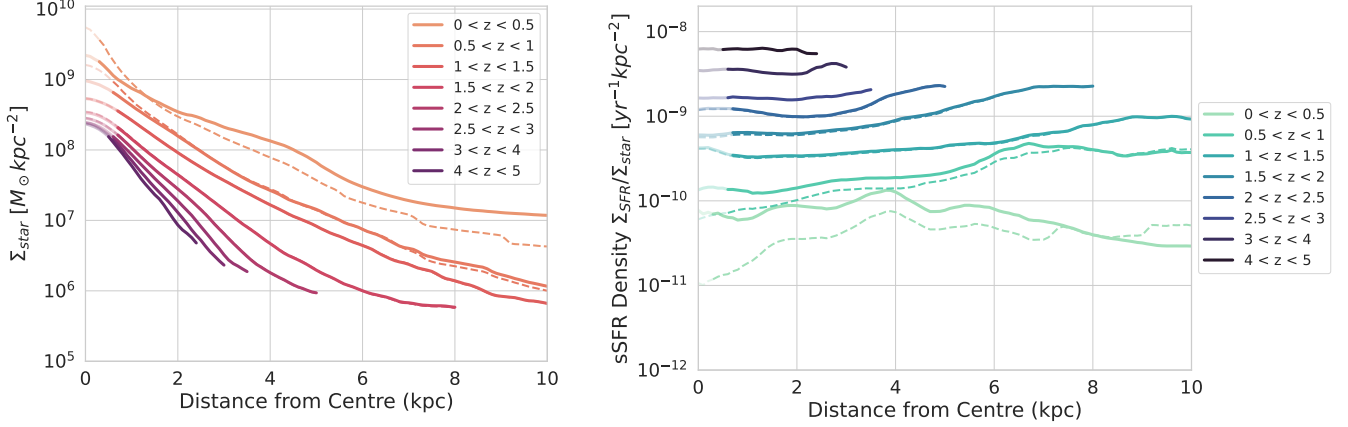


Figure 6. *Left Panel:* Stacked and normalized stellar mass profiles for each redshift epoch. Solid lines are the representative mass density profiles of *only* the star-forming galaxies in each redshift bin, whereas dashed lines are density profiles including *both* star-forming *and* quiescent galaxies. Profiles are truncated at the boundary where the noise dominates. Transparent sections indicate regions of the density profile affected by the PSF. *Right Panel:* Stacked and normalized sSFR (specific star formation rate) profiles for each redshift epoch. Each sSFR profile was obtained by dividing each normalized SFR profile by the normalized mass profile of the same redshift (see Appendix B). The solid and dashed lines represent the same samples as the left panel. The truncation in radial profile is the same as the left panel.

With the stacked and normalized 1-D profiles representative of each redshift epoch in Figure 6, we divide them into inner and outer regions with a 2 kpc cutoff point. While the 2 kpc cutoff point is most of the galaxy at higher redshift bins, especially $z > 4$, the MW in the current universe has a bulge extent of roughly 2 kpc, and thus this region represents the regions which will eventually *become* the bulge for present day MWAs.

In Figure 7, the outer regions, represented by the blue line on the plots, are shown in the top panels to increase in both stellar mass and in sSFR much faster than the inner regions at higher- z . In fact, the epoch between $2.5 < z < 5$ shows very little stellar mass growth in the inner 2 kpc region – only ~ 0.1 dex – while the outer region increased ~ 1 dex, an order of magnitude from the highest redshift bin to $z \sim 2.25$. Additionally, on the top-right panel of Figure 7, while the overall trend of sSFR for the inner regions is decreasing towards lower- z , the trend in sSFR of the outer regions in fact increases up to $z \sim 2$, around cosmic noon, before it decreases at a steady rate with roughly the same slope as the inner region. This demonstrates the rapid and sustained inside-out growth of this sample of progenitors.

In the bottom-left panel of Figure 7, the total, inner, and outer mass density is plotted as a function of redshift. From $z = 5$ to $z = 2$ the total and the outer mass density are decreasing, while the inner mass density remains constant, or grows slowly. While this seems counter to the stellar mass growth in the top-left panel, recall that the galaxies themselves are also increasing in size. Therefore if the stellar mass is added to the outskirts of the galaxy, and increasing its scale-length, the

decrease in mass density is expected. So this panel is further evidence that the MWA progenitors are growing inside-out. It is important to note that the amount of time between $2 < z < 5$ is roughly 2 Gyr. But in that span of time, the galaxies have grown ten times in stellar mass, and increased in size from $R_e \sim 1.0$ kpc to $R_e \sim 1.8$ kpc (see §5.2 for the measurement of R_e and more information on general morphological evolution). After that growth, however, the inner and outer regions increase in stellar mass density at roughly the same rate (i.e. the slope of the inner and outer mass density lines are very similar). Therefore, the mass is growing proportionally at $z < 2$, which means the growth of the inner and outer regions are in lockstep, which is consistent with previous studies.

The bottom-right panel, which plots the sSFR density over time, shows that there is a difference of roughly one magnitude between inner and outer regions with respect to the sSFR per unit area, but this remains consistent throughout each redshift interval. The slope of the inner Σ_{sSFR} stays consistent with redshift, but the slope of the outer Σ_{sSFR} is noticeably flatter between $2 < z < 3$. At $3 < z < 5$, the slope of the outer Σ_{sSFR} is steeper, but not as steep as the slope at $z < 2$. The changing Σ_{sSFR} of the outer regions may indicate more varied star-formation activity in the outer regions at different epochs of growth. Recall that since this sample is only galaxies with total $S/N \geq 30$, the MWA sample is not mass complete at $z > 3$. Therefore, the stellar mass and especially the sSFR trends at $z > 3$ are only representative of the most massive and highly star-forming MWAs at those epochs. It is possible the flattened slope of the

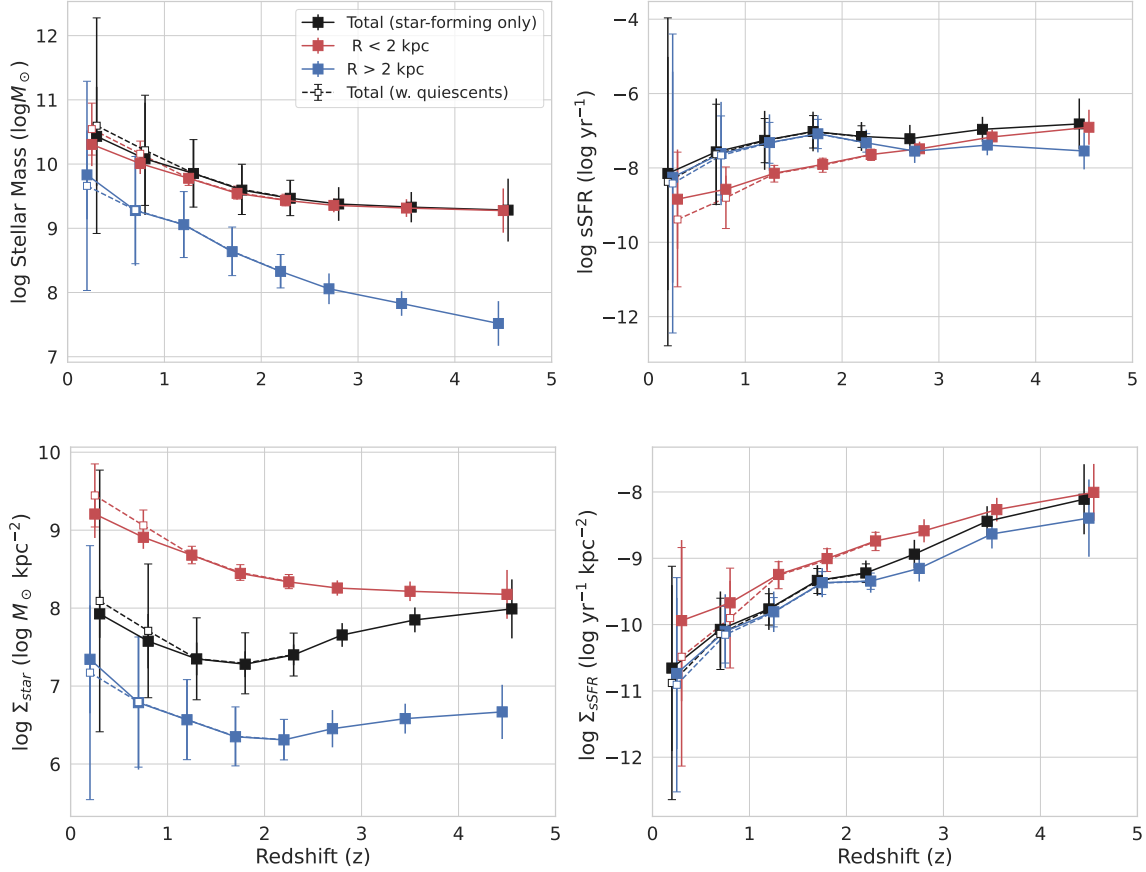


Figure 7. *Top Panels:* Median stellar mass growth on the left, and median specific star formation rate on the right, as a function of redshift. Red and blue show the change in stellar mass or sSFR in the inner ($R < 2$ kpc) and outer ($R > 2$ kpc) regions of the galaxies. Solid lines with filled squares are star-forming galaxies only, dashed lines with white squares represent the median with the quiescent sample included. *Bottom Panels:* Median mass *densities* and median sSFR *densities* as a function of redshift. Error bars in all plots are standard error.

outer Σ_{sSFR} may continue up to $z = 5$ if all possible MWA progenitors were sampled.

4.3. Is SFR the main driver of mass assembly?

We seek to understand the mass growth observed over the redshift ranges that are mass-complete, whether it is dominated by in-situ SFR or if galaxy mergers may play a role. For each redshift bin, we have obtained the median total stellar mass, and the median total SFR. To test if the SFR is consistent with the total mass assembled, we first take the total resolved SFR in units of M_\odot/yr at each redshift bin z_{obs} , and calculate the total mass formed (M_{formed}) by the SFR by integrating over the span of time that has passed.

$$M_{\text{formed}}(z_{\text{obs}}) = \int_{t_i}^{t_f} \text{SFR}_{z_{\text{obs}}}(t) dt, \quad (4)$$

where $\text{SFR}_{z_{\text{obs}}}$ is the median SFR at the redshift epoch z_{obs} , t_i is the age in years of the start of z_{obs} and t_f is the age in years of the end of z_{obs} . Note that for the

median SFR of each redshift range, we only consider star-forming galaxies and ignore quiescent galaxies.

This M_{formed} however does not represent the stellar mass, M_\star that was added in that time period. This is because a portion of the total mass formed is returned to the interstellar medium (ISM), and must be accounted for in our calculations. Therefore, we also take into account the “mass loss” factor, which at its simplest is the percentage of formed mass that becomes stellar mass.

For every redshift epoch, we define the stellar mass that is *not* returned to the ISM as

$$M_{\star\text{added}}(z_{\text{obs}}) = \int_{t_i}^{t_f} \text{SFR}_{z_{\text{obs}}}(t) f_{\text{ret}}(t) dt, \quad (5)$$

where $f_{\text{ret}}(t)$ is the mass-loss curve from FSPS (Conroy & Gunn 2010) that is implemented in Dense Basis to calculate SFHs from the posteriors. At redshifts of $0.5 < z < 5$, the mass loss rate is roughly $\sim 37\%$ to $\sim 43\%$, with higher mass loss at higher- z .

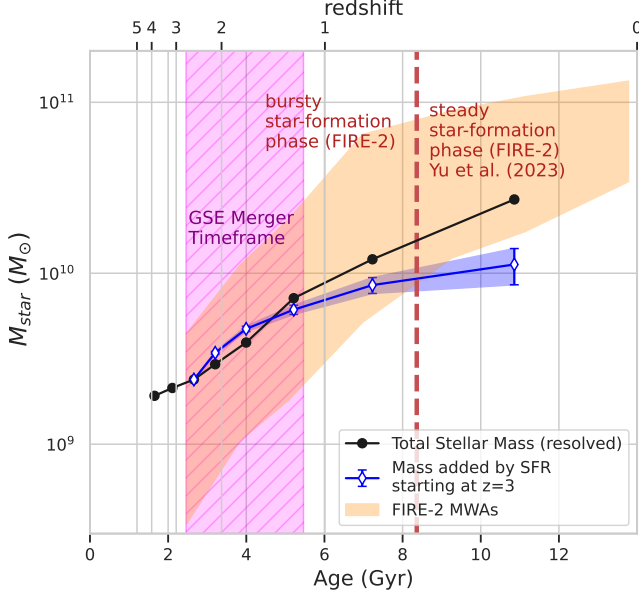


Figure 8. Total mass growth from resolved stellar mass maps (black line, same as black line in Fig. 7). The blue line with white diamonds represents the mass added by the total SFR at each redshift bin since $z = 3$. Orange shaded region is the range of MW-type stellar masses in FIRE-2 as a function of redshift and age in Gyr, (Garrison-Kimmel et al. 2018). Dashed red vertical line denotes demarcation point between bursty star formation and steady star formation in FIRE-2 MW-type galaxies in Yu et al. (2023). Purple shaded region indicates the time frame of the Gaia-Enceladus merger (Belokurov et al. 2018; Helmi et al. 2018)

The SFR-derived $M_{\star,added}$ is then combined with the $M_{initial}$ at the starting redshift. The starting redshift point is at $z = 3$, therefore $M_{initial} \equiv M_{obs,z=3} = 2.4 \times 10^9 M_{\odot}$, and every subsequent redshift epoch:

$$M_{\star,added}(z_{obs}) = M_{obs,z=3} + \int_{t_i}^{t_f} \text{SFR}_{z_{obs}}(t) f_{ret}(t) dt, \quad (6)$$

where the integral represents all of the $M_{\star,added}$ generated from integrating each median SFR at the respective redshift ranges (t_i to t_f) that they cover, with the mass loss factor f_{ret} applied. The comparison of this added stellar mass growth versus the *observed* stellar mass growth (i.e. the median total resolved stellar mass measured at each redshift bin) is presented in Figure 8.

Although we have SFR measurements since $z = 5$, we only integrate the stellar mass added by each median SFR at each time step since $z = 3$. That is because the MWA progenitor sample is complete to $z = 3$, as seen in Figure 2, but due to the aforementioned $S/N = 30$ cut-off, the sample is incomplete beyond $z = 3$. This means

we are only sampling the most massive and most highly star-forming galaxies at $3 < z < 5$, so using the median SFR at those times would bias the calculation. This limits the mass assembly test to a shorter time frame, but disk formation may have only formally started at ~ 12 Gyr ago (Belokurov & Kravtsov 2022), which does correspond to a redshift of $z = 3$.

In Figure 8, the resulting mass added line, plotted in blue with white diamonds, has good agreement with the observed total stellar mass built up since $z = 3$, displayed as the black line. There is a slight discrepancy where the observed SFR builds too much stellar mass at earlier times, but adds too little stellar mass at later times. Clearly, SFR cannot be greater than the mass added. However, derived quantities such as SFR and stellar mass have systematics in their derivation (i.e. see Kennicutt 1998 and Conroy 2013 for in-depth discussions of deriving physical quantities from SEDs and stellar population models). Additionally, it is well-known that the cosmic SFR density over-predicts the observed cosmic stellar mass density (Madau & Dickinson 2014). Integrated SFRs are typically biased higher than stellar mass. Nevertheless, the observed SFR since $z = 3$ to $z \sim 1.5$ adds stellar mass at a rate consistent with solely in-situ star formation. However, the mass added by integrating the observed SFR over time is unable to match the observed total M_{\star} at later epochs, implying some of the stellar mass added may be ex-situ. Heightened star-formation activity can also be induced by merger events, and starbursts may also reduce star-formation in later times due to stellar feedback. The last major merger of the Milky Way, Gaia-Enceladus (GSE), is indicated in Figure 8 as the purple shaded region. The time frame of GSE is estimated to have occurred 8 – 11 Gyr ago (Helmi et al. 2018), or at redshift $1 \lesssim z \lesssim 2.5$. The point in Figure 8 at which the mass added by observed SFR is no longer enough to account for the observed M_{\star} occurs within the GSE merger time frame.

We compare our results to recent MWA simulations from FIRE-2. The orange shaded region in Figure 8 is the range of stellar masses for FIRE-2 MWAs (Garrison-Kimmel et al. 2018). The turning point between bursty and steady phase star formation from Yu et al. (2023) is also included as the vertical dashed red line at a look-back time of ~ 5 Gyr. Both the observed total stellar mass, and the added stellar mass line since $z = 3$ agree with the stellar mass growth from FIRE-2.

5. MORPHOLOGICAL MEASUREMENTS OF MWA PROGENITORS

Examining the morphology of the stellar mass maps can not only strengthen the arguments for inside-out

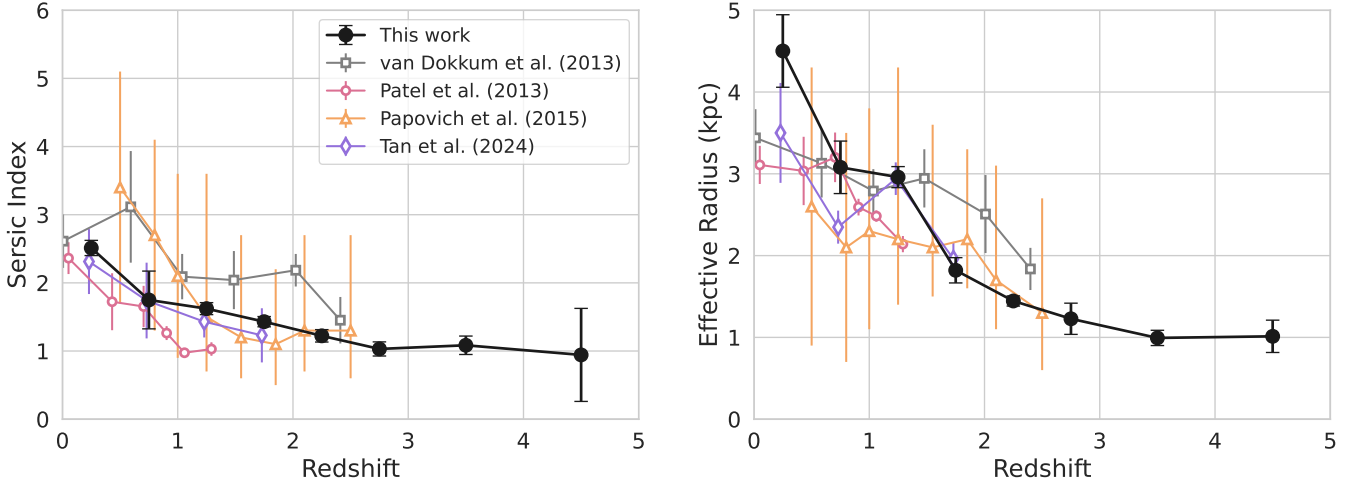


Figure 9. *Left:* Median Sérsic index for each redshift bin. Solid black squares represent this sample of MWA progenitors from CANUCS. *Right:* Median half-mass radius R_e of each redshift bin in kpc, converted via angular diameter distance from photometric redshifts. Error bars represent the standard error in each redshift bin. Other lines are Sérsic parameter measurements from other studies: van Dokkum et al. (2013) in grey, Patel et al. (2013) in pink, Papovich et al. (2015) in orange, and Tan et al. (2024) in purple.

growth of disks at early epochs, but also reveal whether disturbances in structure which resulted from galaxy interactions or mergers have played key roles in mass assembly apart from in-situ star formation.

For the morphological measurements, we utilize Statmorph (Rodríguez-Gomez et al. 2019), a tool developed for asymmetry measurements and clump detection for galaxies. We run Statmorph on the stellar mass maps, the SFR maps, and the F444W maps.

Resolved maps are prepared for Statmorph in a similar manner as described in Tan et al. (2022) and Tan et al. (2024) for morphological fitting.

- We take the corresponding segmentation map of each object from the catalog to define the foreground and the background pixels.
- Noise is added to the stellar mass and SFR maps according to the FWHM of the background noise present in the F444W cutout, using the segmap of the galaxy from the catalog.
- The input PSF is the F444W PSF, since all of the photometry has been PSF-matched to F444W, which means the stellar mass and SFR maps would have the same resolution as F444W.
- A high value was set for gain to allow Statmorph to generate its own weight map for the images, as the provided weight map from the catalog would not apply to derived stellar mass and SFR quantities.

5.1. Sérsic profiles

A Sérsic profile (Sérsic 1963) is a function with two main parameters, n the Sérsic index, and R_e the effective radius, or the radius that contains half of the flux (or in this case, half of the stellar mass).

$$I(R) = I_0 \exp \left(-b_n \left[(R/R_e)^{1/n} - 1 \right] \right) \quad (7)$$

When $n = 1$, the Sérsic profile is purely exponential, and indicates that the surface brightness profile of the galaxy is likely an exponential disk. When $n = 4$, the Sérsic profile likely resembles a de Vaucouleurs profile, and indicates that the galaxy may be bulge-dominated, and elliptical in morphology. Most galaxies are in-between $n = 1$ and $n = 4$, as galaxies usually consist of both a bulge and a disk component.

Statmorph utilizes astropy’s `2DSersic` function and scipy’s `curve-fitting` package to fit either single or double Sérsic profiles to galaxy images. Similar to Galfit (Peng et al. 2010), it takes in a galaxy image and a PSF kernel as input. When tested on fitting F444W photometry of MWA progenitors from the A370NCF field, Statmorph returned similar Sérsic profiles to Galfit when fitted to the same galaxy image, but has lower failure rates. We utilize the fitted Sérsic profile to the spatially resolved stellar mass maps to study general trends in the changes of the morphology of MWAs over cosmic time.

5.2. Sérsic parameters of MWA progenitors since $z = 5$

In Figure 9, the median Sérsic index of each redshift bin is plotted in the left panel, while the median R_e (half-mass radius) is plotted in the right panel. From $3 < z < 5$, the median Sérsic index remains constant at $n \sim 1$, and from $1.5 < z < 3$, the Sérsic index only grows

to a value of $n = 1.62 \pm 0.09$. Within the same redshift ranges, the median R_e , representing the median half-mass radius of the MWA progenitors, is also increasing. In the same time frame of $2 < z < 5$, the R_e increases from 1.0 ± 0.2 kpc at $4 < z < 5$ to 1.84 ± 0.16 kpc at $1.5 < z < 2$.

While it appears at first glance as if both Sérsic index and half-mass radius are not increasing dramatically, it is only true for the Sérsic index. This is because a galaxy with a Sérsic index of $n \sim 1.6$ is still likely disk-dominated, while an increase in half-mass radius from 1.0 kpc to 1.8 kpc is representative of the galaxy’s size almost doubling in the same span of time. As noted in §4.2, the redshift range $2 < z < 5$ is the same epoch where the MWA progenitors exhibit inside-out growth, where more stellar mass is accumulated in the outskirts of the galaxy versus in the inner regions, according to the density profiles in Figure 6 and in Figure 7. This is further proof that the disks are growing, because half-mass radius corresponds to size, while the roughly constant Sérsic index shows that the progenitors are not increasing their central density. Thus they are likely disk-dominated systems.

The next stage of mass assembly takes place from $z = 2$ to $z = 0.3$, and the mass density profiles transition from inside-out growth to proportional mass build-up in both inner and outer regions. As discussed in §4.2, this is the epoch where the change in mass density is equivalent for both inner and outer regions. Figure 9 shows the median Sérsic index at later times does indeed increase up to $n = 2.42 \pm 0.42$ at $0.3 < z < 0.5$. While it is impossible to directly measure the Sérsic index of the MW from an internal vantage point, the bulge-to-total mass ratio of the MW is measured to be $B/T = 0.15$ by Licquia & Newman (2015). Using conversions derived by Brennan et al. (2015) between B/T ratios and Sérsic indices, if the radius of the bulge to the radius of the disk is < 0.4 , the Sérsic index of a galaxy with $B/T = 0.15$ is likely to be $n \lesssim 2$. Therefore, our Sérsic index measurement of $n \sim 2.4$ for the lowest- z progenitors is similar to that expected for the MW. Furthermore, consensus on the MW’s bulge is that its structure is a box/peanut or “X-shaped” bulge (see e.g. Barbuy et al. 2018; Helmi 2020), rather than a classical bulge that is typically described by a de Vaucouleurs profile.

Over the same redshift range, the median half-mass radius increases from $R_e = 1.8 \pm 0.2$ kpc to $R_e = 4.1 \pm 0.3$ kpc at $0.3 < z < 0.5$. This effective radius is comparable to the measurement of the MW’s effective radius from Zhou et al. (2023) at $R_e = 4\text{--}4.5$ kpc, assuming an exponential scale length of the disk of 2.7 kpc from Licquia & Newman (2015). This is another doubling in the average

size of MWA progenitors from $z = 2$ to $z = 0.3$, but over a longer time scale, ~ 7 Gyr. The Sérsic index, while it has increased, is still below $n = 4$, the limit at which a galaxy is then considered bulge-dominated. This means that MWA progenitors remain disk-dominated systems, which is expected. Although our MWA sample is chosen only as analogs in mass, the lowest-redshift MWAs in our sample have sizes and Sérsic indices similar to the Milky Way, suggesting they are also structurally analogs of the Milky Way as well.

5.3. Gini-M20 Statistics

For our sample of galaxies, fitting a single Sérsic profile to the main galaxy in each cutout has its limitations. Sérsic profiles can only reveal the most general information about the flux distribution (or in our case the mass distribution) of the galaxy that it is fit to, and fails to capture the finer structures, such as clumps, tails, or spiral arms. Fitting the unique, finer structures of over 900 galaxies is unfeasible, but there are statistical methods to quantify the overall “clumpiness” of a galaxy image. One such method is via Gini-M20 statistics.

The Gini-M20 plane (Lotz et al. 2004) is another morphology tool which utilizes the relative flux distribution of galaxy images and the contribution of each pixel to the flux to quantify galaxy morphology. It is exceptionally useful for picking out double peaks which can either indicate pairs of merging galaxies, or star-forming clumps, depending on the filter used.

The Gini coefficient was first used for astronomical image classification by Abraham et al. (2003). It is defined for a set of n pixels each with individual flux values I_i as:

$$G = \frac{1}{\bar{I}n(n-1)} \sum_{i=1}^n (2i - n - 1)I_i, \quad (8)$$

where \bar{I} is the average flux of all the pixels. The Gini coefficient is defined in a way such that the values range from 0 to 1, with $G = 0$ assigned to an image with a completely uniform flux, and $G = 1$ assigned to a field with a single bright pixel, and all other pixels containing zero flux. One limitation of the Gini coefficient is that the surface brightness of galaxies is highly redshift dependent. So the implementation of the Gini coefficient calculation in Lotz et al. (2004) and in Statmorph is to construct a Gini segmentation map, which only depends on the Petrosian radius (Petrosian 1976), and is insensitive to redshift. The Petrosian radius R_p is defined as the radius at which the surface brightness $\mu(r)$ at R_p is equal to the mean surface brightness $\bar{\mu}$ contained within R_p , and the ratio of the two values is defined in Lotz et al. (2004) as:

$$\eta = \frac{\mu(R_p)}{\bar{\mu}(r < R_p)} \quad (9)$$

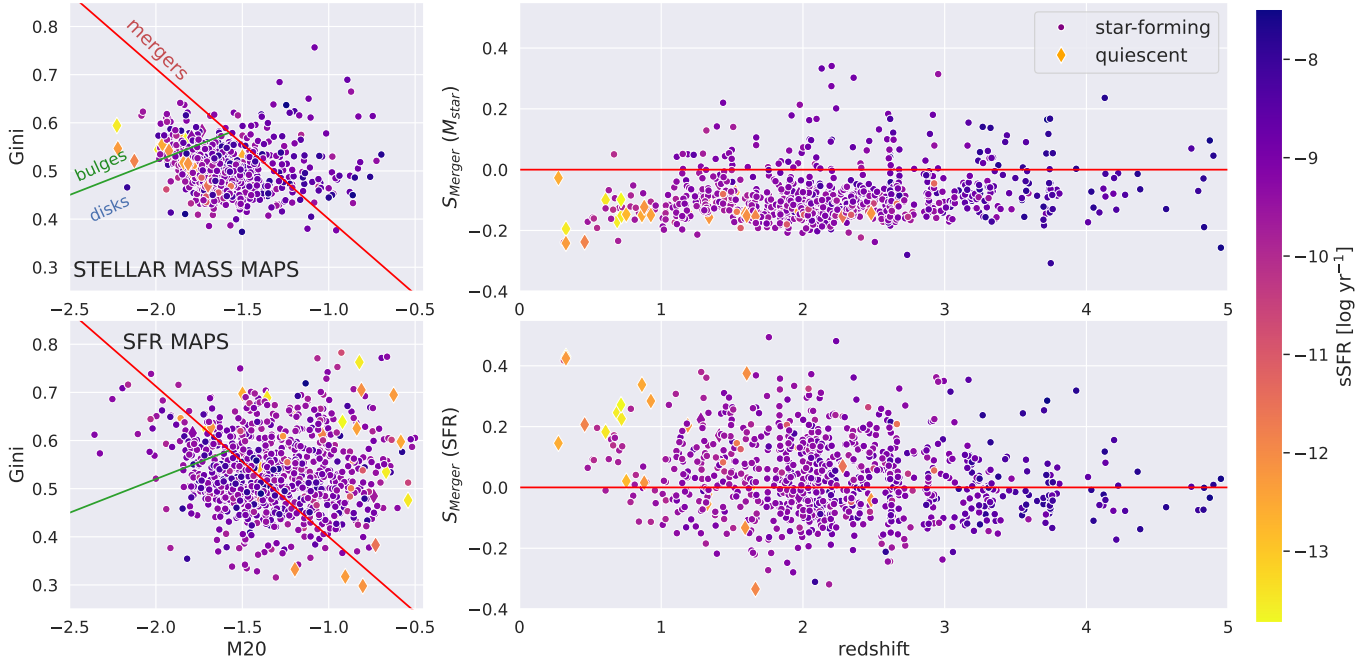


Figure 10. *Left Panels:* Gini- M_{20} plots of the stellar mass distributions (top) and SFR maps (bottom) of the MWA progenitors. *Right Panels:* The Merger Statistic S_{merger} of the MWA progenitors as a function of redshift, for both the stellar mass maps and the SFR maps. Color represents the sSFR of each galaxy. Circular points are the star-forming sample, while diamonds are the quiescent sample. The red line represents the separation between the galaxies with a positive merger statistic, versus the galaxies with a negative merger statistic (S_{merger}). The line is defined in Equation 12. The green line represents the division between bulge-dominated and disk-dominated galaxies. Galaxies with low sSFR, or quiescents, are all clustered around the bulge region of the Gini- M_{20} plane for their *stellar mass maps*, however, the quiescents have an extremely high scatter in the SFR maps.

The default η for the Petrosian radius calculation in Statmorph is set to 0.2.

The M_{20} statistic is the second moment of a galaxy’s brightest pixels, which contains 20% of the total flux, relative to the total second order central moment μ_{tot} . For an image with n pixels located at positions (I_i, y_i) with (x_c, y_c) defined as the galactic centre, μ_{tot} is defined as:

$$\mu_{tot} = \sum_{i=1}^n \mu_i \equiv \sum_{i=1}^n I_i [(x_i - x_c)^2 + (y_i - y_c)^2], \quad (10)$$

where I_i is the flux of an individual pixel. Then, M_{20} is defined as

$$M_{20} \equiv \log_{10} \left(\frac{\sum_i \mu_i}{\mu_{tot}} \right), \sum_i < 0.2 I_{tot}, \quad (11)$$

where I_{tot} is the total flux of the area defined by the segmentation map of the galaxy. Generally, a lower value of M_{20} indicates higher flux concentration. However, unlike the Gini coefficient, M_{20} is not measured on circular or elliptical apertures, and the centre of a galaxy is left as a free parameter. M_{20} also scales with r^2 which makes it more sensitive to detecting multiple spatially resolved bright regions.

Results are presented in the Gini- M_{20} plane, where different regions of the plane identify roughly the morphology of the galaxy. The Gini- M_{20} planes for the stellar mass maps and the SFR maps of the MWA progenitors are shown in the left half of Figure 10. One key region of the Gini- M_{20} plane is the top-right half, where both Gini and M_{20} are high. The galaxies in this region exhibit more than one bright peak in its flux distribution (or in our case, in its stellar mass or SFR distribution), and are thus more likely to be ongoing mergers. However, the interpretation of whether an object in that region is truly a merger is highly dependent on the filter used. Galaxies with satellites, star-forming clumps, and spiral arms can be factors that increase the S_{merger} of a galaxy’s image.

Since we are using the Gini- M_{20} plane on a dataset that spans many redshifts, we define a new dividing line from which to measure the merger statistic. This is because the default S_{merger} from Statmorph is based on the data that [Rodriguez-Gomez et al. \(2019\)](#) were using for their studies, which was comparisons of the Pan-STARRS survey to simulated IllustrisTNG galaxies. We defined a new line for the Gini- M_{20} plane based on visual inspection that the images classified as having a positive

S_{merger} indeed has more than one distinct bright peak in its distribution. The equation that defines the new dividing line is:

$$S_{merger}(G, M_{20}) = 0.322M_{20} + 1.030G - 0.090. \quad (12)$$

In Figure 10, one should note that a high S_{merger} measurement for a galaxy’s SFR map does not necessarily indicate that the galaxy is an ongoing merger. As can be seen from the quiescent galaxies on the SFR map Gini-M20 plane, it has a high scatter, and many quiescent galaxies have a very positive S_{merger} in the SFR, but no quiescent galaxy has a positive S_{merger} in the stellar mass. Gini-M20 statistics only pick out which pixels or groups of pixels are the brightest, but if a galaxy is quiescent, their brightest pixels in the SFR map will not have as high an SFR as an actively star-forming galaxy. Therefore, the utility of using Gini-M20, specifically S_{merger} on SFR maps to classify clumpy versus non-clumpy morphology has limited use case. Therefore, we use the S_{merger} measured on the stellar mass distribution to estimate merger rates with respect to redshift in §5.5. The implications of the utility of S_{merger} measured on SFR distributions is further discussed in §5.6

5.4. Asymmetry measurements

Asymmetry is sensitive to structures such as tidal disturbances, dust lanes, clumpy structures, and double cores. Asymmetry is correlated to mergers, but depending on the stage of the merger, the galaxy may not be highly asymmetric (late stage mergers for instance, do not exhibit great asymmetry). Nevertheless, asymmetry is a useful parameter for detecting disturbances in the process of galaxy evolution, which correlates with merger rate and with galaxy pair interactions.

The most well-known asymmetry parameter comes from the CAS (concentration, asymmetry, smoothness) classification system as described in (Conselice 2003). Statmorph calculates the asymmetry parameter by subtracting the galaxy’s image rotated 180 degrees from its original image:

$$A_{CAS} = \frac{\sum_{i,j} |I_{ij} - I_{ij}^{180}|}{\sum_{i,j} |I_{ij}|} - A_{sky}, \quad (13)$$

where I_{ij} and I_{ij}^{180} are pixel flux values of the original and rotated images, and A_{sky} is the average asymmetry of the sky background.

An alternative measurement of asymmetry is RMS asymmetry, which was introduced in Conselice et al. (2000). An updated version of RMS asymmetry from Sazonova et al. (2024) is currently implemented in the

latest version of Statmorph:

$$A_{RMS}^2 = \frac{\sum_{i,j} (I_{ij} - I_{ij}^{180})^2 - 2\sigma_{sky}^2}{\sum_{i,j} I_{ij}^2 - \sigma_{sky}^2}, \quad (14)$$

where σ_{sky} is the RMS noise of the background.

Sazonova et al. (2024) argues that RMS asymmetry is a more robust asymmetry measurement as it is fully independent from noise and aperture size. However, both A_{CAS} and A_{RMS} are correlated to image resolution. Since our study compares galaxies across a wide span of redshifts, it is of the utmost importance that the *physical resolution scale* (i.e. the kpc scale per pixel) is the same.

5.5. Mergers and disturbed galaxies at high redshift

For the rest of our analysis, we focus mainly on the morphological measurements of stellar mass maps. We choose three different proxies for merger rate: S_{merger} from the Gini-M20 plane, CAS asymmetry (A_{CAS}), and RMS asymmetry (A_{RMS}).

We compare the merger statistic, CAS asymmetry, and RMS asymmetry for the galaxies’ stellar mass maps in both their original resolution (which is the same resolution as the F444W photometry) versus the images that have been matched the the same *physical resolution* via the angular diameter distance obtained at each object’s redshift. Therefore, the images that have been resolution-matched have one pixel represent the exact same physical extent of the galaxy with the poorest resolution (at $z \sim 1.6$, where the angular diameter distance vs. redshift reverses in our cosmology). This resolution is 0.339 kpc per pixel.

We define the merger fraction morphologically with the stellar mass maps. we use the fraction of galaxies with $S_{merger} > 0$ in stellar mass to determine the “merger candidate fraction” (Lotz et al. 2008b). The merger statistic is a reasonable predictor of “true” ongoing mergers, as shown from comparisons of the correlation of the value of S_{merger} on mock observation images of galaxy mergers at different stages produced from simulations (i.e. Lotz et al. 2008a; Snyder et al. 2015a,b; Rodriguez-Gomez et al. 2019). For our purposes, we use merger fraction synonymously with merger candidate fraction, but we note that it is not a true “merger fraction”.

In the top row of Figure 11, we plot the median S_{merger} , A_{CAS} and A_{RMS} as a function of redshift, while in the bottom row of the same figure, we plot the merger fractions and disturbed fractions. For all parameters, both the median parameter based on the original stellar mass maps, and the median parameter based on the resolution-matched stellar mass maps, increase

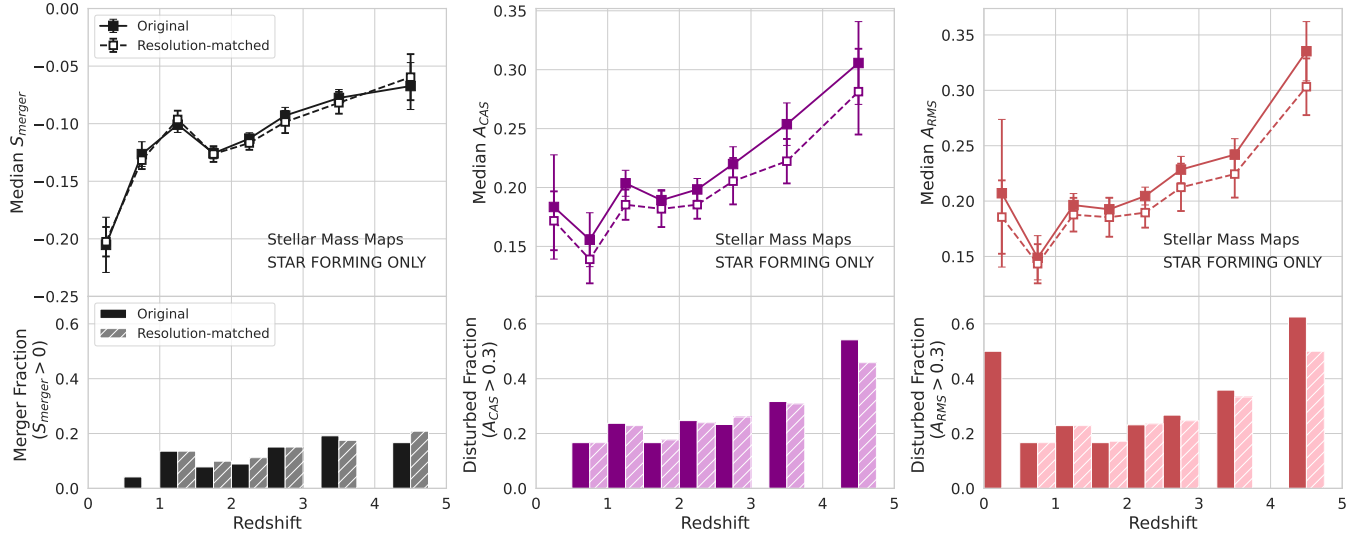


Figure 11. *Top:* From left to right, the median S_{merger} , A_{CAS} , and A_{RMS} for each redshift bin. In each top panel, the solid lines with filled squares represent the median of the distribution as measured from the original resolution of the stellar mass maps, and the dashed lines with unfilled squares represent the median from the *resolution matched* stellar mass maps. *Bottom:* Left panel is merger fraction as determined by number of galaxies per redshift that has $S_{merger} > 0$. Center and right panels are “disturbed” fractions, determined by galaxies with $A_{CAS} > 0.3$ or $A_{RMS} > 0.3$ respectively. In all cases, resolution matching decreases the fraction of disturbed galaxies, but increases the merger fraction at the highest and lowest redshift bins.

with redshift. Though the resolution-matched parameters tend to be slightly lower, with the difference increasing with redshift (as expected, since angular resolution for this sample is increasing with redshift). There is a similar trend with the merger fractions (derived from number of galaxies with $S_{merger} > 0$, as seen on the top-right panel of Figure 10) and disturbed fractions, derived from either $A_{CAS} > 0.3$ or $A_{RMS} > 0.3$ for each redshift bin. The division line was chosen to be 0.3 because the median A_{CAS} and A_{RMS} are both ~ 0.3 at the highest redshift bin.

The merger fraction on the whole follows a downward trajectory, and the peak S_{merger} is $19.3 \pm 4.0\%$ at $3 < z < 4$ for the original resolution stellar mass maps, and $20.8 \pm 9.3\%$ at $4 < z < 5$ for the resolution-matched stellar mass maps. This demonstrates that in general, the rate of active, ongoing mergers increases with redshift, and there were more frequent mergers in the past, as we approach the epoch of reionization. This is also supported by the disturbed fraction also increasing with redshift, whether the fraction is measured based on A_{CAS} or A_{RMS} . The maximum of the resolution-matched disturbed fraction based on A_{CAS} is $45.8 \pm 13.8\%$ and the maximum disturbed fraction based on A_{RMS} is $50.0 \pm 14.4\%$, both found at the highest redshift bin ($4 < z < 5$). Since asymmetry accounts for disturbances to galaxy structure, there is a slight upward trend at the lowest redshift bin.

5.6. Overlap of star-forming regions with stellar mass distribution

As stated earlier in §5.3, S_{merger} is, in this case, a measurement of the likelihood that an image contains double or multiple peaks. Therefore, if we use S_{merger} on the SFR maps, then it could be a generalized measurement for whether a galaxy is clumpy in star formation. However, $S_{merger, SFR}$ does not reveal any information about where the clumps are located, or the intensity of the star formation (i.e. the burstiness of the star formation). Due to these limitations, we utilize an alternative method to measure clump fraction for our sample. This is based on the clump detection methods outlined in Sok et al. (2022) using rest-frame u -band images of galaxies, based on the method developed by Wuyts et al. (2012), and refined in Sok et al. (2024) for both rest-frame u -band and stellar mass maps. In addition, we also measure the similarity between the stellar mass map and the SFR map for each galaxy using the Normalized Mutual Information index (NMI, Studholme et al. 1999) between the stellar mass maps and SFR maps. The more correlated two images are, the higher the NMI, and the more similar the SFR distribution is to the stellar mass distribution.

In Figure 12, we plot both the median NMI between stellar mass and SFR maps in the top-left, and the clumpiness fractions in the bottom left. Both clumpy fraction measurements show a similar trend of decreasing with redshift. The clumpiness fractional being in-

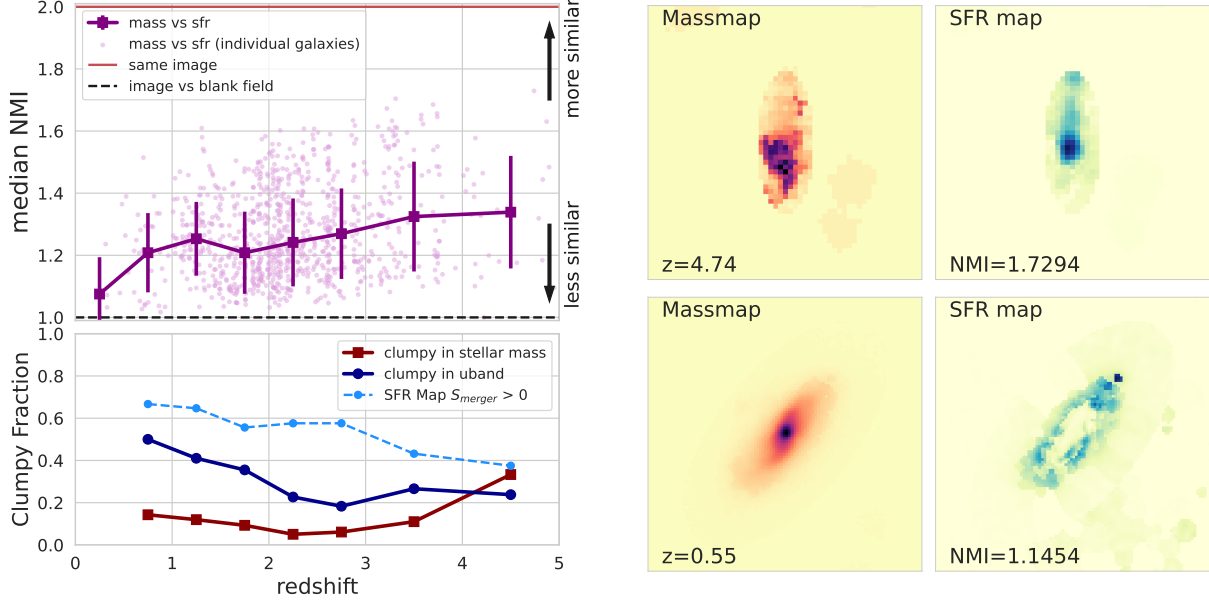


Figure 12. *Top-Left:* Normalized mutual information (NMI) comparing mass maps to SFR maps for each MWA progenitor (purple points). The median NMI at each redshift bin is plotted as the purple line, with the error bars as 1σ of the distribution. Red line indicates an NMI of 2, where two images are identical. Dashed black line indicates an NMI of 1, when any non-blank image is compared to a blank field. Median NMI decreases with redshift, showing that the SFR maps are more similar to mass maps at earlier times than at later times. *Bottom-Left:* Clumpy fraction as a function of redshift, as determined by the clump-finding algorithm from Sok et al. (2024) for u -band in dark blue, and stellar mass maps in dark red. Stellar mass clumpiness fraction correlates to Stellar mass merger statistic and merger fraction in Figure 11. Likewise, u -band clumpiness fraction correlates to SFR clumpiness fraction, also determined by $S_{merger} > 0$ (dotted light blue line). *Right Panel:* Example of a high- z galaxy with a high NMI (top) and a low- z galaxy with a low NMI (bottom). These figures show that while fraction of galaxies that are clumpy in u -band or SFR increases with decreasing redshift, the amount of area covered by the clumpy star-forming regions make up less of the galaxies’ total surface area as well, as seen in the decreasing NMI.

versely proportional to redshift seems counter to models of star formation and disk assembly. We note however, that it is clear from the results outlined in §4 that star formation is much greater at earlier times. Therefore, we include the NMI measurement to see if the regions where star formation rate is occurring correspond to regions of higher stellar mass. In the median NMI, the correlation between the SFR maps and the stellar mass maps are decreasing with redshift. Furthermore, we show two example galaxies, one at high- z and one at low- z , to show that indeed, the SFR maps are more similar to stellar mass maps at earlier times.

From this, we can infer that at early times, such as the galaxy that is at $z = 4.74$ in the top-right figure, regions of bursty star formation correspond more to where the stellar mass is. In that sense, it is not that bursty star formation is less clumpy, but that both SFR and stellar mass are *both clumpy* at higher- z . But once more stellar mass is set in place, the star-forming regions make up less and less of the galaxy, and eventually only form in the outskirts of the galaxy, which is evidenced by the bottom right images of the galaxy at $z = 0.57$, where the SFR, while technically “clumpy”, does not correspond

to the smooth stellar mass distribution, and is also much lower than at high- z .

6. DISCUSSION

Semi-analytic galaxy simulations (such as Benincasa et al. 2020; Grudić et al. 2023; Yu et al. 2023; Pinna et al. 2024; Semenov et al. 2024) have just begin to explore the question of how exactly the MW’s disk formed and evolved, especially as we have evidence that a subset of the stars in the MW’s thick disk originated from a major merger that occurred 8-11 Gyr ago known as Gaia-Enceladus (GSE merger). We will consider how the CANUCS sample of observed MWAs compares to previous simulation-based studies of MWA formation.

Recall that in §4.3, we compared the total mass growth of the CANUCS MWAs to the mass growth of MWAs in FIRE-2. Specifically, we included the study of thin and thick disk formation using FIRE-2 MWAs presented in Yu et al. (2023), where the authors tracked the kinematic and morphological evolution of star particles within twelve simulated MWAs. This SFR turning point from Yu et al. (2023), which occurs at ~ 5 Gyr ($z \sim 0.5$) and is plotted in Figure 8, is significant be-

cause it is also when their simulated galaxies switch from assembling the thick disk to assembling the thin disk. In our sample, the timing of the turning point corresponds to the largest jump in the half-mass radius (R_e , right panel of Figure 9), where R_e increases from 2.5 kpc to 4.1 kpc. This means the size growth in the last ~ 5 Gyr of the MWAs happened during this “steady phase” of star formation and occurred in the outskirts of the galaxies (as demonstrated in Figures 6 and 7, as well as on the right panel of Figure 12), and this growth may be the equivalent of thin disk assembly in MWAs.

Although we find strong evidence for inside-out growth as well as disk assembly with our MWA sample, our mass map derived morphology parameters exhibit both opposing and agreeable trends to Yu et al. (2023). The Sérsic index of our sample increases with decreasing redshift, showing that our MWAs are becoming more *bulge-dominated* at later times, even after removing quiescent galaxies. In contrast, the circularity of stellar orbits for the FIRE-2 MWAs in Yu et al. (2023) (which they use as a proxy for disk-like morphology) increases with decreasing redshift, showing their mass distributions are becoming more *disk-dominated* at later times.

Another simulation-based study with MWAs in TNG50 from Sotillo-Ramos et al. (2022) tracked both in-situ SFR and “diskiness” (measured via D/T or disk-to-total mass ratio) over time, and found that increased in-situ SFR is associated with increased diskiness of the MWAs. Their definition of disk is also dependent upon circularity ($\epsilon > 0.7$ for the disks). However, a major merger episode will disrupt diskiness, but still increase in-situ SFR (in a starburst), with the disks reforming afterwards (the orbits of the newly formed stars settling into circular orbits). It can be argued that the generally decreasing trend of the merger and disturbed fractions of the CANUCS MWAs is evidence of this settling down after the starbursts that occurred at $z > 3$. The timescale of the disk reformation according to Sotillo-Ramos et al. (2022) is anywhere from < 1 Gyr to ~ 2 Gyr. If a redshift bin covers a span of time that is $\gtrsim 1$ Gyr, then it is more likely the median Sérsic index n in our observed MWA sample will average out all of the morphology of the merging and non-merger galaxies and return a disk-like value close to $n = 1$.

6.1. Star formation, mergers, and morphology

On the other hand, A_{CAS} , A_{RMS} , and S_{merger} of the CANUCS MWA progenitors all show an increasing trend with *increasing* redshift. Asymmetry parameters are correlated with galaxy pair interactions and tidal features, both of which contribute to turbulence and non-circular orbits. Ultimately, Sérsic profiles are

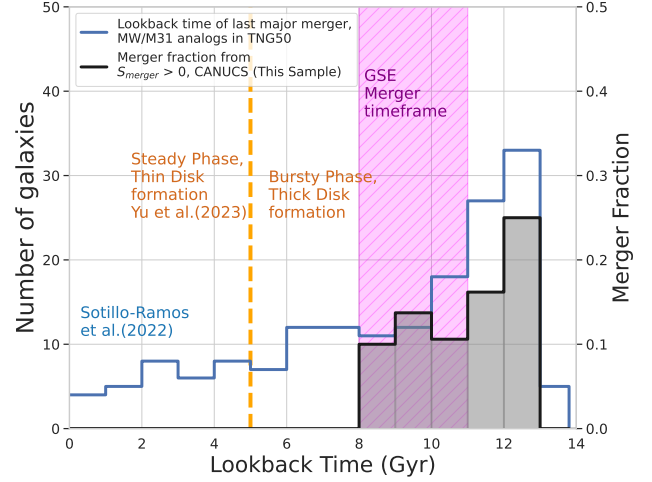


Figure 13. The lookback time of last major merger in TNG50 MWAs (blue line, Sotillo-Ramos et al. 2022) compared to the merger fraction at each lookback time for CANUCS MWAs (black line, grey shading). The time frame at which the GSE merger occurred is shaded purple (Helmi et al. 2018). Orange dashed line at 5 Gyr indicates transition from thick disk formation to thin disk formation (Yu et al. 2023).

derived from surface brightness, which is not related to orbit circularity. Meanwhile, asymmetry parameters are more closely related to orbital circularity, and thus similar trends appear between observation and simulation.

6.2. Merger rates over time

The time frame of the last major merger of the MW, the GSE merger, corresponds to a redshift of $1 < z < 2.5$. This is an interesting epoch because all of the parameters that track merger rates plotted in Figure 11 appear to show an upturn at $1 < z < 2$, despite the overall decreasing trend of merger rates and asymmetry with decreasing redshift. This upturn is the most pronounced for the merger statistic, plotted on the left panels, where the merger fraction at $1 < z < 1.5$ is $\sim 14.0 \pm 3.4\%$.

In Figure 13, we re-bin the merger fraction defined by $S_{merger} > 0$ of CANUCS MWA progenitors, from the bottom-left panel of Figure 11, by lookback time instead of redshift (black solid line with grey shading). The peak of the merger fraction as broken down by lookback time is 12-13 Gyr ago, corresponding to redshifts $z > 3$, as expected. Interestingly, the merger fractions as a function of lookback time no longer has the drastic upturn that appears when binned by redshift. We compare the CANUCS MWA merger fraction with results from TNG50, specifically Sotillo-Ramos et al. (2022), as they focused on disk survival rates of MWAs that experienced major mergers. The number of MWAs in

TNG50 for which their last major merger occurred at a certain lookback time is also plotted in Figure 13 as the blue dashed line. The CANUCS MWA merger fractions also agree well with the distribution of last major merger occurrence versus lookback time from the TNG50 MWAs. Note that this is *not* a one-to-one comparison of occurrence rates of mergers. Simulations have access to the full star formation histories of each galaxy, and know when, and how many mergers occurred. Observational results are snapshots of various galaxies at only one point in their evolutionary history.

Since certain redshift epochs correspond to the formation of different regions of the MW or other similar disk galaxies, the abundance-matched progenitors observed at that redshift will reveal what environments or interactions may have assembled these structures. The thin disk, as the outermost structure with the youngest stellar populations appear to be formed via steady star formation at the outskirts of a fully formed disk galaxy at $z < 1$ (Yu et al. 2023). Unless a major merger takes place after the steady phase of star formation sets in (such as with M31, see D’Souza & Bell 2018), this steady star formation will not disrupt the morphology of the thin disk. The thick disk, however, formed before and during cosmic noon ($1 \lesssim z \lesssim 3$), where we see burstier star formation and more chances of mergers: events that would dynamically heat the forming disk. Mergers may disrupt or even destroy disks (Sotillo-Ramos et al. 2022), but the disk is able to reform given enough time, albeit with larger scale heights. Before the formation of the thick disk, the bulge would form in a very early universe with much more density, and far more major mergers. Systems like the Sunrise arc (Vanzella et al. 2023), Firefly Sparkle (Mowla et al. 2024), and Cosmic Gems (Adamo et al. 2024; Bradley et al. 2024), are among the first glimpses into the highly chaotic formation of the central regions of much more rotationally supported “grand design” spiral galaxies in the present universe.

7. SUMMARY

We used abundance matching on all ten fields of the CANUCS catalogs to find a sample of 909 spatially resolved MWA progenitors since $z = 5$. The stellar mass ranges of these galaxies match well with both simulations and previous observation-based studies of MWA evolution. We then performed resolved SED-fitting with Dense Basis to create stellar mass and SFR maps of our MWA progenitors in order to track the mass assembly, sSFR, and morphology evolution. Our main results are as follows:

- There is strong evidence of inside-out growth for the selected MWA progenitors before $z = 2$. From

the mass density profiles (Figures 6 and 7), we find that at $2 < z < 5$, the M_* in the outer regions ($R > 2$ kpc) grows by 0.8 dex, which is eight times more than the M_* growth in the inner regions (0.1 dex within $R < 2$ kpc). The maximum sSFR of each stacked and normalized sSFR profile in Figure 6 from $z \sim 4$ to $z \sim 0.5$ is located at or close to the furthest point from the profile’s center. The sSFR of the inner regions in Figure 7 decrease steadily since $z = 5$, while the sSFR of the outer regions increase between $2 < z < 5$, matching the inner regions at $z \sim 3$, and only begin to decrease after cosmic noon ($z \sim 1.75$).

- Additionally, in Figure 9, the median Sérsic indices of the MWA progenitors demonstrate that up to $z \sim 0.5$, these galaxies remain highly disk-dominated systems. Meanwhile, the change in their median half-mass radius implies that the progenitors are doubling in size from $z \sim 5$ to $z \sim 3$, and again from $z \sim 3$ to $z \sim 0.3$. The lack of strong evolution in Sérsic index combined with steady growth in R_e imply the galaxies are building their disks inside-out at earlier times.
- The merger rates of our MWA progenitors are defined using the position of the galaxy’s mass map on the Gini-M20 plane ($S_{merger} > 0$, Figure 10). The most conservative merger fraction at $4 < z < 5$ is $16.7 \pm 8.3\%$ (Figure 11). Between $45.8 \pm 13.8\%$ to $62.5 \pm 16.1\%$ of MWA progenitors at $4 < z < 5$ are classified as disturbed, using either CAS or RMS asymmetry. Merger fractions and disturbed fractions have an overall decreasing trend with redshift. The mass growth of early galaxies likely involve frequent interactions and higher merger rates than low- z galaxies.
- The clumpiness of the stellar mass maps is higher at high- z , especially $4 < z < 5$, but remains at $< 20\%$ at $z < 4$ (Figure 12). Although the clumpiness of the SFR maps increases towards lower- z , the overall SFR decreases, so the star-forming clumps at lower- z are less bursty than their higher- z counterparts. There is also more mismatch between regions of high SFR and the underlying stellar mass distribution. This means that highly star-forming regions at higher- z are more likely to be located where there is more stellar mass, whereas the star-forming regions at low- z usually are found in regions with lower mass density. MWAs evolve from small, disturbed systems with extreme star formation activity to a large disk with pockets of

star formation that surround a massive, quiescent bulge.

Since both SFR and asymmetry of the CANUCS MWA progenitors all increase as z increases, this matches simulations of MWA evolution where disk galaxies exhibit burstier star formation at earlier times that leads to less circularized/more eccentric and thus more “asymmetric” stellar orbits. Therefore, the thick disk of MWAs in general may be formed either via bursty episodes of star formation that dynamically heat a less massive disk, or via mergers disrupting the disk or inducing a starburst as the galaxy forms.

8. ACKNOWLEDGMENTS

This research was supported by grant 18JWST-GTO1 and 23JWGO2A13 from the Canadian Space Agency

(CSA), and funding from the Natural Sciences and Engineering Research Council of Canada (NSERC). The MAST DOI for CANUCS is [doi:10.17909/ph4n-6n76](https://doi.org/10.17909/ph4n-6n76). J. A-D. is supported by the Natural Sciences and Engineering Research Council of Canada (NSERC). Y.A. is supported by a Research Fellowship for Young Scientists from the Japan Society of the Promotion of Science (JSPS). This research used the Canadian Advanced Network For Astronomy Research (CANFAR) operated in partnership by the Canadian Astronomy Data Centre and The Digital Research Alliance of Canada with support from the National Research Council of Canada the Canadian Space Agency, CANARIE, and the Canadian Foundation for Innovation.

REFERENCES

- Abadi, M. G., Navarro, J. F., Steinmetz, M., & Eke, V. R. 2003, *ApJ*, 597, 21, doi: [10.1086/378316](https://doi.org/10.1086/378316)
- Abraham, R. G., van den Bergh, S., & Nair, P. 2003, *ApJ*, 588, 218, doi: [10.1086/373919](https://doi.org/10.1086/373919)
- Adamo, A., Bradley, L. D., Vanzella, E., et al. 2024, arXiv e-prints, arXiv:2401.03224, doi: [10.48550/arXiv.2401.03224](https://doi.org/10.48550/arXiv.2401.03224)
- Antwi-Danso, J., Papovich, C., Leja, J., et al. 2023, *ApJ*, 943, 166, doi: [10.3847/1538-4357/aca294](https://doi.org/10.3847/1538-4357/aca294)
- Asada, Y., Sawicki, M., Abraham, R., et al. 2024a, *MNRAS*, 527, 11372, doi: [10.1093/mnras/stad3902](https://doi.org/10.1093/mnras/stad3902)
- Asada, Y., Desprez, G., Willott, C. J., et al. 2024b, arXiv e-prints, arXiv:2410.21543, doi: [10.48550/arXiv.2410.21543](https://doi.org/10.48550/arXiv.2410.21543)
- Barbuy, B., Chiappini, C., & Gerhard, O. 2018, *ARA&A*, 56, 223, doi: [10.1146/annurev-astro-081817-051826](https://doi.org/10.1146/annurev-astro-081817-051826)
- Behroozi, P. S., Marchesini, D., Wechsler, R. H., et al. 2013, *ApJL*, 777, L10, doi: [10.1088/2041-8205/777/1/L10](https://doi.org/10.1088/2041-8205/777/1/L10)
- Belli, S., Newman, A. B., & Ellis, R. S. 2019, *ApJ*, 874, 17, doi: [10.3847/1538-4357/ab07af](https://doi.org/10.3847/1538-4357/ab07af)
- Belokurov, V., Erkal, D., Evans, N. W., Koposov, S. E., & Deason, A. J. 2018, *MNRAS*, 478, 611, doi: [10.1093/mnras/sty982](https://doi.org/10.1093/mnras/sty982)
- Belokurov, V., & Kravtsov, A. 2022, *MNRAS*, 514, 689, doi: [10.1093/mnras/stac1267](https://doi.org/10.1093/mnras/stac1267)
- Benincasa, S. M., Loebman, S. R., Wetzel, A., et al. 2020, *MNRAS*, 497, 3993, doi: [10.1093/mnras/staa2116](https://doi.org/10.1093/mnras/staa2116)
- Bensby, T., Feltzing, S., & Lundström, I. 2003, *A&A*, 410, 527, doi: [10.1051/0004-6361:20031213](https://doi.org/10.1051/0004-6361:20031213)
- Bertin, E., & Arnouts, S. 1996, *A&AS*, 117, 393, doi: [10.1051/aas:1996164](https://doi.org/10.1051/aas:1996164)
- Bignone, L. A., Helmi, A., & Tissera, P. B. 2019, *ApJL*, 883, L5, doi: [10.3847/2041-8213/ab3e0e](https://doi.org/10.3847/2041-8213/ab3e0e)
- Bland-Hawthorn, J., & Gerhard, O. 2016, *ARA&A*, 54, 529, doi: [10.1146/annurev-astro-081915-023441](https://doi.org/10.1146/annurev-astro-081915-023441)
- Boardman, N., Zasowski, G., Seth, A., et al. 2020a, *MNRAS*, 491, 3672, doi: [10.1093/mnras/stz3126](https://doi.org/10.1093/mnras/stz3126)
- Boardman, N., Zasowski, G., Newman, J. A., et al. 2020b, *MNRAS*, 498, 4943, doi: [10.1093/mnras/staa2731](https://doi.org/10.1093/mnras/staa2731)
- Bovy, J., & Rix, H.-W. 2013, *ApJ*, 779, 115, doi: [10.1088/0004-637X/779/2/115](https://doi.org/10.1088/0004-637X/779/2/115)
- Bradley, L., Sipocz, B., Robitaille, T., et al. 2016, Photutils: Photometry tools, Astrophysics Source Code Library, record ascl:1609.011
- Bradley, L., Sipocz, B., Robitaille, T., et al. 2023, astropy/photutils: 1.10.0, 1.10.0, Zenodo, doi: [10.5281/zenodo.1035865](https://doi.org/10.5281/zenodo.1035865)
- Bradley, L. D., Adamo, A., Vanzella, E., et al. 2024, arXiv e-prints, arXiv:2404.10770, doi: [10.48550/arXiv.2404.10770](https://doi.org/10.48550/arXiv.2404.10770)
- Brammer, G. B., van Dokkum, P. G., & Coppi, P. 2008, *ApJ*, 686, 1503, doi: [10.1086/591786](https://doi.org/10.1086/591786)
- Brennan, R., Pandya, V., Somerville, R. S., et al. 2015, *MNRAS*, 451, 2933, doi: [10.1093/mnras/stv1007](https://doi.org/10.1093/mnras/stv1007)
- Buck, T., Obreja, A., Macciò, A. V., et al. 2020, *MNRAS*, 491, 3461, doi: [10.1093/mnras/stz3241](https://doi.org/10.1093/mnras/stz3241)
- Calzetti, D., Armus, L., Bohlin, R. C., et al. 2000, *ApJ*, 533, 682, doi: [10.1086/308692](https://doi.org/10.1086/308692)
- Cappellari, M., & Copin, Y. 2003, *MNRAS*, 342, 345, doi: [10.1046/j.1365-8711.2003.06541.x](https://doi.org/10.1046/j.1365-8711.2003.06541.x)
- Chabrier, G. 2003, *PASP*, 115, 763, doi: [10.1086/376392](https://doi.org/10.1086/376392)

- Conroy, C. 2013, *ARA&A*, 51, 393,
doi: [10.1146/annurev-astro-082812-141017](https://doi.org/10.1146/annurev-astro-082812-141017)
- Conroy, C., & Gunn, J. E. 2010, *ApJ*, 712, 833,
doi: [10.1088/0004-637X/712/2/833](https://doi.org/10.1088/0004-637X/712/2/833)
- Conselice, C. J. 2003, *ApJS*, 147, 1, doi: [10.1086/375001](https://doi.org/10.1086/375001)
- Conselice, C. J., Bershadsky, M. A., & Jangren, A. 2000,
ApJ, 529, 886, doi: [10.1086/308300](https://doi.org/10.1086/308300)
- Costantin, L., Pérez-González, P. G., Guo, Y., et al. 2023,
Nature, 623, 499, doi: [10.1038/s41586-023-06636-x](https://doi.org/10.1038/s41586-023-06636-x)
- Desprez, G., Martis, N. S., Asada, Y., et al. 2024, *MNRAS*,
530, 2935, doi: [10.1093/mnras/stae1084](https://doi.org/10.1093/mnras/stae1084)
- D’Souza, R., & Bell, E. F. 2018, *Nature Astronomy*, 2,
737–743, doi: [10.1038/s41550-018-0533-x](https://doi.org/10.1038/s41550-018-0533-x)
- Engler, C., Pillepich, A., Joshi, G. D., et al. 2023, *MNRAS*,
522, 5946, doi: [10.1093/mnras/stad1357](https://doi.org/10.1093/mnras/stad1357)
- Estrada-Carpenter, V., Sawicki, M., Brammer, G., et al.
2024, *MNRAS*, 532, 577, doi: [10.1093/mnras/stae1368](https://doi.org/10.1093/mnras/stae1368)
- Fraser-McKelvie, A., Merrifield, M., & Aragón-Salamanca,
A. 2019, *MNRAS*, 489, 5030, doi: [10.1093/mnras/stz2493](https://doi.org/10.1093/mnras/stz2493)
- Fuhrmann, K. 2011, *MNRAS*, 414, 2893,
doi: [10.1111/j.1365-2966.2011.18476.x](https://doi.org/10.1111/j.1365-2966.2011.18476.x)
- Garrison-Kimmel, S., Hopkins, P. F., Wetzel, A., et al.
2018, *MNRAS*, 481, 4133, doi: [10.1093/mnras/sty2513](https://doi.org/10.1093/mnras/sty2513)
- Giménez-Arteaga, C., Oesch, P. A., Brammer, G. B., et al.
2023, *ApJ*, 948, 126, doi: [10.3847/1538-4357/acc5ea](https://doi.org/10.3847/1538-4357/acc5ea)
- Gledhill, R., Strait, V., Desprez, G., et al. 2024, *arXiv*
e-prints, arXiv:2403.07062,
doi: [10.48550/arXiv.2403.07062](https://doi.org/10.48550/arXiv.2403.07062)
- Goddard, D., Thomas, D., Maraston, C., et al. 2017,
MNRAS, 466, 4731, doi: [10.1093/mnras/stw3371](https://doi.org/10.1093/mnras/stw3371)
- Grand, R. J. J., Gómez, F. A., Marinacci, F., et al. 2017,
MNRAS, 467, 179, doi: [10.1093/mnras/stx071](https://doi.org/10.1093/mnras/stx071)
- Grazian, A., Fontana, A., Santini, P., et al. 2015, *A&A*,
575, A96, doi: [10.1051/0004-6361/201424750](https://doi.org/10.1051/0004-6361/201424750)
- Grudić, M. Y., Hafen, Z., Rodriguez, C. L., et al. 2023,
MNRAS, 519, 1366, doi: [10.1093/mnras/stac3573](https://doi.org/10.1093/mnras/stac3573)
- Guedes, J., Callegari, S., Madau, P., & Mayer, L. 2011,
ApJ, 742, 76, doi: [10.1088/0004-637X/742/2/76](https://doi.org/10.1088/0004-637X/742/2/76)
- Helmi, A. 2020, *ARA&A*, 58, 205,
doi: [10.1146/annurev-astro-032620-021917](https://doi.org/10.1146/annurev-astro-032620-021917)
- Helmi, A., Babusiaux, C., Koppelman, H. H., et al. 2018,
Nature, 563, 85, doi: [10.1038/s41586-018-0625-x](https://doi.org/10.1038/s41586-018-0625-x)
- Hopkins, P. F. 2015, *MNRAS*, 450, 53,
doi: [10.1093/mnras/stv195](https://doi.org/10.1093/mnras/stv195)
- Hopkins, P. F., Wetzel, A., Kereš, D., et al. 2018, *MNRAS*,
480, 800, doi: [10.1093/mnras/sty1690](https://doi.org/10.1093/mnras/sty1690)
- Horta, D., & Schiavon, R. P. 2024, *arXiv* e-prints,
arXiv:2404.16939, doi: [10.48550/arXiv.2404.16939](https://doi.org/10.48550/arXiv.2404.16939)
- Iyer, K., & Gawiser, E. 2017, *ApJ*, 838, 127,
doi: [10.3847/1538-4357/aa63f0](https://doi.org/10.3847/1538-4357/aa63f0)
- Iyer, K. G., Gawiser, E., Faber, S. M., et al. 2019, *ApJ*,
879, 116, doi: [10.3847/1538-4357/ab2052](https://doi.org/10.3847/1538-4357/ab2052)
- Kennicutt, Robert C., J. 1998, *ARA&A*, 36, 189,
doi: [10.1146/annurev.astro.36.1.189](https://doi.org/10.1146/annurev.astro.36.1.189)
- Kilic, M., Munn, J. A., Harris, H. C., et al. 2017, *ApJ*, 837,
162, doi: [10.3847/1538-4357/aa62a5](https://doi.org/10.3847/1538-4357/aa62a5)
- Kormendy, J., & Bender, R. 2019, *ApJ*, 872, 106,
doi: [10.3847/1538-4357/aafdf](https://doi.org/10.3847/1538-4357/aafdf)
- Le Conte, Z. A., Gadotti, D. A., Ferreira, L., et al. 2024,
MNRAS, 530, 1984, doi: [10.1093/mnras/stae921](https://doi.org/10.1093/mnras/stae921)
- Licquia, T. C., & Newman, J. A. 2015, *ApJ*, 806, 96,
doi: [10.1088/0004-637X/806/1/96](https://doi.org/10.1088/0004-637X/806/1/96)
- Licquia, T. C., Newman, J. A., & Bershadsky, M. A. 2016,
ApJ, 833, 220, doi: [10.3847/1538-4357/833/2/220](https://doi.org/10.3847/1538-4357/833/2/220)
- Licquia, T. C., Newman, J. A., & Brinchmann, J. 2015,
ApJ, 809, 96, doi: [10.1088/0004-637X/809/1/96](https://doi.org/10.1088/0004-637X/809/1/96)
- Lotz, J. M., Jonsson, P., Cox, T. J., & Primack, J. R.
2008a, *MNRAS*, 391, 1137,
doi: [10.1111/j.1365-2966.2008.14004.x](https://doi.org/10.1111/j.1365-2966.2008.14004.x)
- Lotz, J. M., Primack, J., & Madau, P. 2004, *AJ*, 128, 163,
doi: [10.1086/421849](https://doi.org/10.1086/421849)
- Lotz, J. M., Davis, M., Faber, S. M., et al. 2008b, *ApJ*, 672,
177, doi: [10.1086/523659](https://doi.org/10.1086/523659)
- Lotz, J. M., Koekemoer, A., Coe, D., et al. 2017, *ApJ*, 837,
97, doi: [10.3847/1538-4357/837/1/97](https://doi.org/10.3847/1538-4357/837/1/97)
- Madau, P., & Dickinson, M. 2014, *ARA&A*, 52, 415,
doi: [10.1146/annurev-astro-081811-125615](https://doi.org/10.1146/annurev-astro-081811-125615)
- McLeod, D. J., McLure, R. J., Dunlop, J. S., et al. 2021,
MNRAS, 503, 4413, doi: [10.1093/mnras/stab731](https://doi.org/10.1093/mnras/stab731)
- Moster, B. P., Naab, T., & White, S. D. M. 2018, *MNRAS*,
477, 1822, doi: [10.1093/mnras/sty655](https://doi.org/10.1093/mnras/sty655)
- Mowla, L., Iyer, K., Asada, Y., et al. 2024, *arXiv* e-prints,
arXiv:2402.08696, doi: [10.48550/arXiv.2402.08696](https://doi.org/10.48550/arXiv.2402.08696)
- Muñoz-Mateos, J. C., Gil de Paz, A., Boissier, S., et al.
2007, *ApJ*, 658, 1006, doi: [10.1086/511812](https://doi.org/10.1086/511812)
- Mutch, S. J., Croton, D. J., & Poole, G. B. 2011, *ApJ*, 736,
84, doi: [10.1088/0004-637X/736/2/84](https://doi.org/10.1088/0004-637X/736/2/84)
- Muzzin, A., Marchesini, D., Stefanon, M., et al. 2013, *ApJ*,
777, 18, doi: [10.1088/0004-637X/777/1/18](https://doi.org/10.1088/0004-637X/777/1/18)
- Noirot, G., Desprez, G., Asada, Y., et al. 2023, *MNRAS*,
525, 1867, doi: [10.1093/mnras/stad1019](https://doi.org/10.1093/mnras/stad1019)
- Oñorbe, J., Boylan-Kolchin, M., Bullock, J. S., et al. 2015,
MNRAS, 454, 2092, doi: [10.1093/mnras/stv2072](https://doi.org/10.1093/mnras/stv2072)
- Papovich, C., Labbé, I., Quadri, R., et al. 2015, *ApJ*, 803,
26, doi: [10.1088/0004-637X/803/1/26](https://doi.org/10.1088/0004-637X/803/1/26)
- Patel, S. G., Fumagalli, M., Franx, M., et al. 2013, *ApJ*,
778, 115, doi: [10.1088/0004-637X/778/2/115](https://doi.org/10.1088/0004-637X/778/2/115)
- Peng, C. Y., Ho, L. C., Impey, C. D., & Rix, H.-W. 2010,
AJ, 139, 2097, doi: [10.1088/0004-6256/139/6/2097](https://doi.org/10.1088/0004-6256/139/6/2097)

- Petrosian, V. 1976, *ApJL*, 210, L53,
doi: [10.1086/18230110.1086/182253](https://doi.org/10.1086/18230110.1086/182253)
- Pillepich, A., Nelson, D., Springel, V., et al. 2019, *MNRAS*, 490, 3196, doi: [10.1093/mnras/stz2338](https://doi.org/10.1093/mnras/stz2338)
- Pillepich, A., Sotillo-Ramos, D., Ramesh, R., et al. 2023, arXiv e-prints, arXiv:2303.16217,
doi: [10.48550/arXiv.2303.16217](https://doi.org/10.48550/arXiv.2303.16217)
- Pinna, F., Grand, R. J. J., Martig, M., & Fragkoudi, F. 2024, *A&A*, 691, A61, doi: [10.1051/0004-6361/202450843](https://doi.org/10.1051/0004-6361/202450843)
- Portail, M., Gerhard, O., Wegg, C., & Ness, M. 2017, *MNRAS*, 465, 1621, doi: [10.1093/mnras/stw2819](https://doi.org/10.1093/mnras/stw2819)
- Rihtaršič, G., Bradač, M., Desprez, G., et al. 2024, arXiv e-prints, arXiv:2406.10332,
doi: [10.48550/arXiv.2406.10332](https://doi.org/10.48550/arXiv.2406.10332)
- Rodriguez-Gomez, V., Snyder, G. F., Lotz, J. M., et al. 2019, *MNRAS*, 483, 4140, doi: [10.1093/mnras/sty3345](https://doi.org/10.1093/mnras/sty3345)
- Rusta, E., Salvadori, S., Gelli, V., Koutsouridou, I., & Marconi, A. 2024, arXiv e-prints, arXiv:2407.06255,
doi: [10.48550/arXiv.2407.06255](https://doi.org/10.48550/arXiv.2407.06255)
- Salvadori, S., Ferrara, A., Schneider, R., Scannapieco, E., & Kawata, D. 2010, *MNRAS*, 401, L5,
doi: [10.1111/j.1745-3933.2009.00772.x](https://doi.org/10.1111/j.1745-3933.2009.00772.x)
- Santini, P., Fontana, A., Castellano, M., et al. 2017, *ApJ*, 847, 76, doi: [10.3847/1538-4357/aa8874](https://doi.org/10.3847/1538-4357/aa8874)
- Sarrouh, G. T., Muzzin, A., Iyer, K. G., et al. 2024, arXiv e-prints, arXiv:2401.08781,
doi: [10.48550/arXiv.2401.08781](https://doi.org/10.48550/arXiv.2401.08781)
- Sazonova, E., Morgan, C., Balogh, M., et al. 2024, arXiv e-prints, arXiv:2404.05792,
doi: [10.48550/arXiv.2404.05792](https://doi.org/10.48550/arXiv.2404.05792)
- Schaye, J., Crain, R. A., Bower, R. G., et al. 2015, *MNRAS*, 446, 521, doi: [10.1093/mnras/stu2058](https://doi.org/10.1093/mnras/stu2058)
- Schreiber, C., Pannella, M., Elbaz, D., et al. 2015, *A&A*, 575, A74, doi: [10.1051/0004-6361/201425017](https://doi.org/10.1051/0004-6361/201425017)
- Semenov, V. A., Conroy, C., Smith, A., Puchwein, E., & Hernquist, L. 2024, arXiv e-prints, arXiv:2409.18173,
doi: [10.48550/arXiv.2409.18173](https://doi.org/10.48550/arXiv.2409.18173)
- Sérsic, J. L. 1963, *Boletín de la Asociación Argentina de Astronomía La Plata Argentina*, 6, 41
- Shen, J., Rich, R. M., Kormendy, J., et al. 2010, *ApJL*, 720, L72, doi: [10.1088/2041-8205/720/1/L72](https://doi.org/10.1088/2041-8205/720/1/L72)
- Snyder, G. F., Lotz, J., Moody, C., et al. 2015a, *MNRAS*, 451, 4290, doi: [10.1093/mnras/stv1231](https://doi.org/10.1093/mnras/stv1231)
- Snyder, G. F., Torrey, P., Lotz, J. M., et al. 2015b, *MNRAS*, 454, 1886, doi: [10.1093/mnras/stv2078](https://doi.org/10.1093/mnras/stv2078)
- Sok, V., Muzzin, A., Jablonka, P., et al. 2022, *ApJ*, 924, 7,
doi: [10.3847/1538-4357/ac2f40](https://doi.org/10.3847/1538-4357/ac2f40)
- . 2024, arXiv e-prints, arXiv:2410.21370,
doi: [10.48550/arXiv.2410.21370](https://doi.org/10.48550/arXiv.2410.21370)
- Sotillo-Ramos, D., Pillepich, A., Donnari, M., et al. 2022, *MNRAS*, 516, 5404, doi: [10.1093/mnras/stac2586](https://doi.org/10.1093/mnras/stac2586)
- Speagle, J. S., Steinhardt, C. L., Capak, P. L., & Silverman, J. D. 2014, *ApJS*, 214, 15,
doi: [10.1088/0067-0049/214/2/15](https://doi.org/10.1088/0067-0049/214/2/15)
- Studholme, C., Hill, D., & Hawkes, D. 1999, *Pattern Recognition*, 32, 71,
doi: [https://doi.org/10.1016/S0031-3203\(98\)00091-0](https://doi.org/https://doi.org/10.1016/S0031-3203(98)00091-0)
- Tan, V. Y. Y., Muzzin, A., Marchesini, D., et al. 2024, arXiv e-prints, arXiv:2402.12433,
doi: [10.48550/arXiv.2402.12433](https://doi.org/10.48550/arXiv.2402.12433)
- Tan, V. Y. Y., Muzzin, A., Marsan, Z. C., et al. 2022, *ApJ*, 933, 30, doi: [10.3847/1538-4357/ac7051](https://doi.org/10.3847/1538-4357/ac7051)
- Tully, R. B., & Fisher, J. R. 1977, *A&A*, 54, 661
- Tumlinson, J. 2010, *ApJ*, 708, 1398,
doi: [10.1088/0004-637X/708/2/1398](https://doi.org/10.1088/0004-637X/708/2/1398)
- van den Bosch, F. C. 1998, *ApJ*, 507, 601,
doi: [10.1086/306354](https://doi.org/10.1086/306354)
- van Dokkum, P. G., Leja, J., Nelson, E. J., et al. 2013, *ApJL*, 771, L35, doi: [10.1088/2041-8205/771/2/L35](https://doi.org/10.1088/2041-8205/771/2/L35)
- Vanzella, E., Claeysens, A., Welch, B., et al. 2023, *ApJ*, 945, 53, doi: [10.3847/1538-4357/acb59a](https://doi.org/10.3847/1538-4357/acb59a)
- Wang, J., Kauffmann, G., Overzier, R., et al. 2011, *MNRAS*, 412, 1081,
doi: [10.1111/j.1365-2966.2010.17962.x](https://doi.org/10.1111/j.1365-2966.2010.17962.x)
- Wegg, C., & Gerhard, O. 2013, *MNRAS*, 435, 1874,
doi: [10.1093/mnras/stt1376](https://doi.org/10.1093/mnras/stt1376)
- Wegg, C., Gerhard, O., & Portail, M. 2015, *MNRAS*, 450, 4050, doi: [10.1093/mnras/stv745](https://doi.org/10.1093/mnras/stv745)
- Wetzel, A. R., Hopkins, P. F., Kim, J.-h., et al. 2016, *ApJL*, 827, L23, doi: [10.3847/2041-8205/827/2/L23](https://doi.org/10.3847/2041-8205/827/2/L23)
- White, S. D. M., & Rees, M. J. 1978, *MNRAS*, 183, 341,
doi: [10.1093/mnras/183.3.341](https://doi.org/10.1093/mnras/183.3.341)
- Wild, V., Taj Aldeen, L., Carnall, A., et al. 2020, *MNRAS*, 494, 529, doi: [10.1093/mnras/staa674](https://doi.org/10.1093/mnras/staa674)
- Williams, R. J., Quadri, R. F., Franx, M., van Dokkum, P., & Labbé, I. 2009, *ApJ*, 691, 1879,
doi: [10.1088/0004-637X/691/2/1879](https://doi.org/10.1088/0004-637X/691/2/1879)
- Willott, C. J., Doyon, R., Albert, L., et al. 2022, *PASP*, 134, 025002, doi: [10.1088/1538-3873/ac5158](https://doi.org/10.1088/1538-3873/ac5158)
- Willott, C. J., Desprez, G., Asada, Y., et al. 2024, *ApJ*, 966, 74, doi: [10.3847/1538-4357/ad35bc](https://doi.org/10.3847/1538-4357/ad35bc)
- Wuyts, S., Förster Schreiber, N. M., Genzel, R., et al. 2012, *ApJ*, 753, 114, doi: [10.1088/0004-637X/753/2/114](https://doi.org/10.1088/0004-637X/753/2/114)
- Xiang, M., & Rix, H.-W. 2022, *Nature*, 603, 599,
doi: [10.1038/s41586-022-04496-5](https://doi.org/10.1038/s41586-022-04496-5)
- Yu, S., Bullock, J. S., Gurvich, A. B., et al. 2023, *MNRAS*, 523, 6220, doi: [10.1093/mnras/stad1806](https://doi.org/10.1093/mnras/stad1806)
- Zhou, S., Aragón-Salamanca, A., Merrifield, M., et al. 2023, *MNRAS*, 521, 5810, doi: [10.1093/mnras/stad853](https://doi.org/10.1093/mnras/stad853)

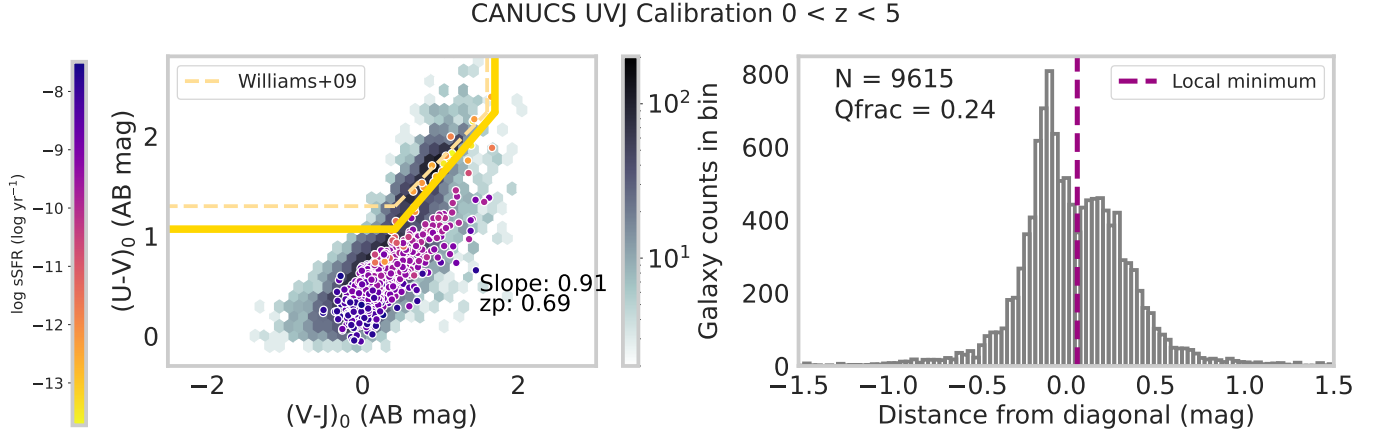


Figure 14. *Left Panel:* Rest-frame UVJ diagram of 9516 galaxies from the CANUCS CLU fields with redshifts $0 < z < 5$ shown as the grey bins. Darker bins indicate higher number count of galaxies. The MWA progenitors are plotted on top, with each circle representing one galaxy, and the color indicating the integrated sSFR. The UVJ boundaries used in this work are shown in yellow with dashed yellow line indicating the UVJ boundaries from Williams et al. (2009). *Right Panel:* Histogram distribution of the same 9516 galaxies and their distance from the diagonal UVJ boundary line. Purple dashed line indicates local minimum, and is analogous to the UVJ diagonal line in the left panel.

APPENDIX

A. UVJ COLOR CALIBRATION FOR THIS DATASET

In §2.4, the UVJ diagram is used to determine the quiescent fraction of potential MWA progenitors and remove them from the analysis. In order to have unbiased UVJ boundaries, we cannot use the MWA progenitor sample itself to determine the boundaries due to the low quiescent fraction and lack of bimodality. Instead, a sample of 9516 galaxies from the cluster fields is used to fit the UVJ boundaries. The slope of the red sequence determines the slope of the calibrated line, and the local minimum of the distribution determines the y -intercept.

In Figure 14, we plot the full sample of galaxies that are used to calibrate the UVJ lines. The original color cuts were generated for every galaxy present in the CLU fields from $0.5 < z < 6$, which we have adjusted to $0 < z < 5$ to match the redshift range of the MWA progenitor sample in this work. The reason the cluster fields are used but not the NCF fields is because there are not enough quiescent galaxies in the NCF fields for a clear bimodal distribution in UVJ color space. The quiescent fraction of the CANUCS sample at $0 < z < 5$ in the NCF fields is only 0.07%, while in the CLU fields it is 24% in the same redshift range due to the presence of the clusters.

B. CREATING 1-D PROFILES

As summarized in §4.1, we created 1-D stellar mass and SFR density profiles by placing down elliptical annuli with width 0.1kpc centered on the stellar mass maps and SFR maps of each respective galaxy. The stacking is performed along the semi-major axis of each galaxy for consistency. Figure 15 is an expanded version of Figure 6 from §4.1. Displayed are each individual galaxy's density profile divided into eight subplots by redshift bin. The stacked and normalized profile is shown in the same color as in Figure 6. The dashed grey lines represent profiles of quiescent galaxies while solid lines are the star-forming galaxies. The dashed colored lines represent the stacked and normalized profile for each redshift bin including both star-forming and quiescents, while the solid colored lines only include star-forming galaxies. The profiles are also not truncated by the noise floor. One difference between Figure 6 and Figure 15 is that the bottom panel of Figure 15 shows the SFR density instead of the sSFR density. Indeed the sSFR density profiles were created via dividing each stacked and normalized SFR density profile at each redshift by its corresponding mass density profile.

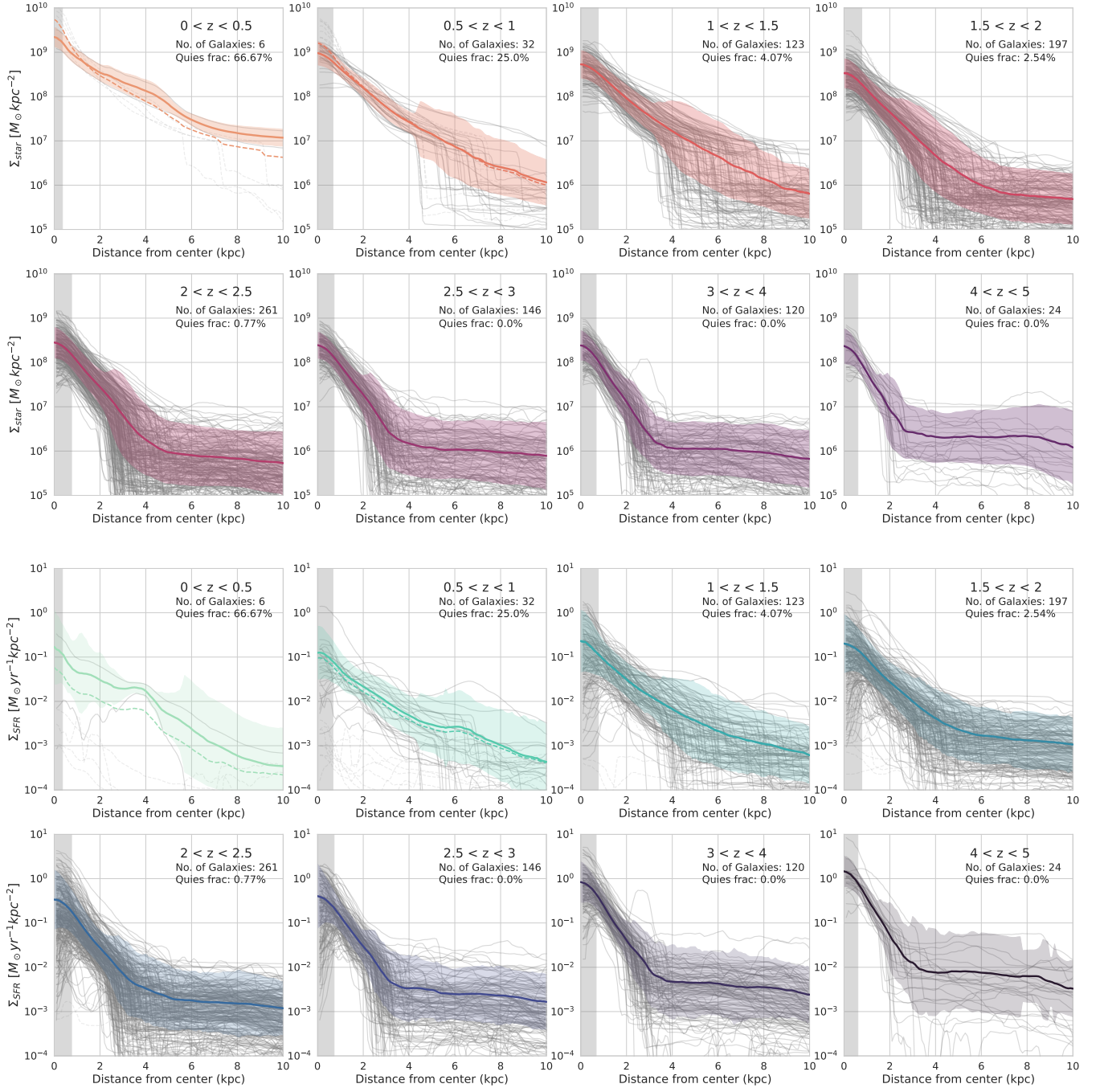


Figure 15. *Top Panel:* 1-D stellar mass density profiles for each MWA, plotted in grey. Colored lines are the stacked and normalized profile of all the galaxies in each redshift bin. Shaded regions represent the 1-sigma (68th percentile) region. The vertical grey shaded region near $R = 0$ kpc represents the average physical size of the PSF FWHM at that redshift bin. *Bottom Panel:* Similar to the plot above but for SFR density profiles. The total number of galaxies per redshift bin, and the quiescent fraction is also displayed in the top-right corner.